NASA
Technical
Paper
3086

May 1991

Numerical Study of the Aerodynamic Effects of Using Sulfur Hexafluoride as a Test Gas in Wind Tunnels

W. Kyle Anderson

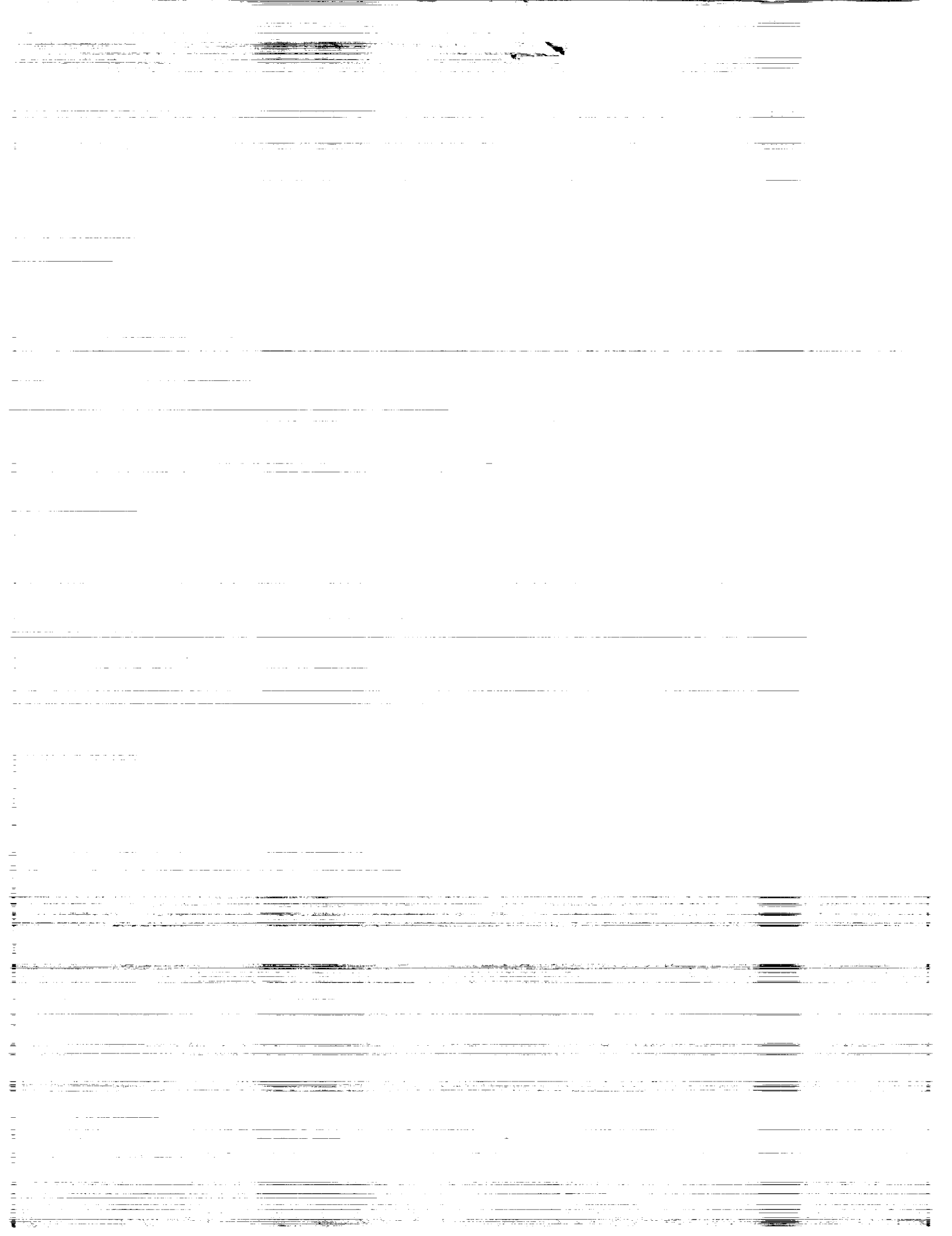

NASA Technical Paper 3086

1991

Numerical Study of the Aerodynamic Effects of Using Sulfur Hexafluoride as a Test Gas in Wind Tunnels

W. Kyle Anderson
Langley Research Center
Hampton, Virginia

NASA
National Aeronautics and Space Administration
Office of Management
Scientific and Technical Information Division

Abstract

A numerical study is presented that investigates some aerodynamic consequences of using sulfur hexafluoride (SF_6) as a test gas in wind tunnels. Inviscid results for airfoils indicate that the shock location calculated for SF_6 is vastly different from that in air for transonic cases. As the free-stream pressure is increased for a given free-stream temperature and Mach number, and real-gas effects become more pronounced, the shock moves progressively forward on the airfoil. Good correlation, however, can be obtained between SF_6 and air even for pressures at which nonideal-gas effects are significant by altering the free-stream SF_6 Mach number using a Mach number scaling procedure.

Computations for subsonic turbulent flows over an NACA 0012 airfoil show that the maximum angle of attack at which steady lift can be obtained is different between air and SF_6. In addition, for SF_6 this angle of attack depends greatly on the free-stream conditions. However, close agreement with air can be achieved at low subsonic Mach numbers by altering the free-stream Mach number according to the inviscid scaling procedure. Conversely, calculated viscous results show that even with Mach number scaling at transonic Mach numbers, the shock location and skin-friction values calculated between air and SF_6 are in disagreement. This is attributed to the limitations of the scaling procedure and to the thinner boundary layer for SF_6.

Introduction

The capability to conduct three-dimensional wind-tunnel testing at full-scale Reynolds numbers has long been seen as an important need for aircraft design. Several of the techniques currently available for achieving high Reynolds numbers include various combinations of high pressure, cryogenic temperatures, and alternate test gases. An additional capability often required is the separation of Mach number and Reynolds number effects since locally high Mach numbers may exist on portions of the model even at relatively low free-stream Mach numbers. Unfortunately, with the exception of the National Transonic Facility (NTF) at the Langley Research Center, which uses cryogenic nitrogen as a test gas, full-scale three-dimensional testing in which both the Mach number and Reynolds number can be varied independently is possible only for a limited number of configurations. Even here, the complexity and cost of models, the time to cool the tunnel, and other complications associated with cryogenic temperatures make the use of the NTF very expensive and cumbersome for the initial development stage of new configurations. These limitations impose severe constraints on the aerodynamic community since only a limited amount of testing at full-scale Reynolds numbers is possible.

In an effort to improve this situation, alternative test gases are being considered that may be used in order to obtain high Reynolds numbers for full-scale, three-dimensional configurations. One such gas is sulfur hexafluoride (SF_6), which is odorless, colorless, nonflammable, nontoxic, and essentially inert (ref. 1). Its high molecular weight makes this gas attractive as an air substitute in order to achieve high Reynolds numbers. Particular interest lies in the use of pressurized wind tunnels since further increases in Reynolds numbers can be achieved and because Reynolds number and Mach number effects can be varied independently. Unfortunately, even at low pressures, sulfur hexafluoride does not behave thermodynamically the same as air. Furthermore, unlike air, SF_6 is a nonideal gas whose internal energy and speed of sound are dependent on both pressure and temperature. Although this is of little consequence for incompressible flows, compressibility effects at higher speeds (such as the variation of shock locations and boundary-layer properties with Mach number) differ between the two gases so that the interpretation of results between air and SF_6 requires investigation.

The purpose of this study is to present numerical results as an aid in determining the suitability of SF_6 as a possible substitute for air in wind tunnels. Nonideal-gas thermodynamic properties for SF_6 are included in both inviscid and viscous calculations. The use of simple scaling procedures for flows over airfoils is examined for correlating the

results obtained in SF_6 with those of air. The method of analysis and the scaling procedure should be generally applicable to other nonideal gases for which the thermodynamic properties are known.

Symbols

A	Helmholtz energy, J/kg; also used for transonic scaling and for stream-tube area
a	speed of sound m/sec
$\bar{a}_i, \bar{b}_i, \bar{c}_i, d$	coefficients for equation of state for SF_6
$\tilde{b}$	defined in equation (15)
C_i	coefficients for curve fit of ideal specific heat C_p
C_p	specific heat at constant pressure, J/kg-K
C_v	specific heat at constant volume, J/kg-K
c	airfoil chord; also Sutherland's constant
c_f	skin-friction coefficient
c_l	lift coefficient
c_p	pressure coefficient
E	total energy per volume, J/m^3
$\mathbf{F}$,$\mathbf{G}$	inviscid fluxes
$\mathbf{G}_v$	viscous flux
H	total enthalpy per mass, J/kg
h	enthalpy per mass, J/kg
K	bulk modulus, N/m^2
k	constant in equation of state for SF_6; also thermal conductivity, N/sec-K
L	Reference length, taken as chord, m
M	Mach number, V/a
N_{Pr}	Prandtl number, $\mu C_p/k$
N_{Re}	Reynolds number, $\rho V L/\mu$
p	pressure, N/m^2 or atm
$\mathbf{Q}$	conservation variables
R	specific gas constant, J/kg-K
S	entropy, J/kg-K
T	temperature, K or °F
t	time, sec
u	velocity in x-direction
$\bar{u}$	velocity normal to outer boundary
V	velocity, m/sec
v	specific volume, m^3/kg; also velocity in y-direction
x, y	Cartesian coordinates, m
Z	compressibility factor
α	angle of attack, deg
β	thermal expansion coefficient, per K
γ	ratio of specific heats
γ'	effective gamma for transonic scaling
δ	boundary-layer thickness, m
δ^*	displacement thickness, m
ϵ	internal energy per mass, J/kg
θ	momentum thickness, m
κ	transonic similarity parameter
λ	coefficient of bulk viscosity, N-sec/m^2
μ	molecular viscosity, N-sec/m^2
ξ, η	general curvilinear coordinates
ρ	density, kg/m^3
τ	thickness parameter

Subscripts:

b	quantity on boundary
c	thermodynamic properties at critical point
i	quantity in first cell interior to outer boundary
ref	reference condition
T	stagnation conditions
x, y	differentiation in x- and y-directions, respectively
∞	infinity

Superscripts:

o	ideal-gas values
*	conditions at $M = 1$
~	nondimensional quantities

Thermodynamic Properties of Sulfur Hexafluoride

The current interest in SF_6 for wind-tunnel applications stems from its high density and low viscosity. At standard conditions ($p_\infty = 1$ atm, $T_\infty = 298$ K), the density of SF_6 is approximately five times that of air and its viscosity is about 20 percent lower (ref. 1). From the equation for Reynolds number

$$N_{Re} = \frac{\rho_\infty V_\infty L}{\mu_\infty} = \frac{\rho_\infty M_\infty a_\infty L}{\mu_\infty} \tag{1}$$

it is seen that both the increased density and the lower viscosity serve to increase the Reynolds number for fixed reference length and velocity. However, the speed of sound for SF_6 is about one-third that of air at these conditions, indicating that the lower speed of sound for a fixed Mach number tends to lessen the increases in Reynolds number obtained from the higher density and lower viscosity. This effect, however, is more than compensated for by the higher density and lower viscosity of SF_6 so that the Reynolds number for SF_6 is more than twice that of air at standard conditions and a fixed Mach number. Figure 1 shows Reynolds number per foot as a function of Mach number for several stagnation pressures and a stagnation temperature of 70° F. For stagnation conditions of 10 atm, Reynolds numbers on the order of 48×10^6 per foot can be obtained at $M = 0.3$, whereas Reynolds numbers higher than 100×10^6 per foot can be achieved at $M = 1$. At a stagnation pressure of 1 atm, Reynolds numbers of about 4.7×10^6 and 10.3×10^6 per foot can be attained for Mach numbers of 0.3 and 1, respectively. At these same stagnation conditions (1 atm, 70°F), the Reynolds number attained in air for $M = 0.3$ is about 2×10^6 per foot and for $M = 1$ is about 4.7×10^6 per foot. Therefore, through the use of SF_6, the Reynolds number increases by a factor of 2.3 at $M = 0.3$ and by a factor of 2.1 at $M = 1$. It is apparent that significant gains in Reynolds number can be achieved by utilizing SF_6 as a test gas in wind tunnels.

In addition to Reynolds number advantages, the low speed of sound of SF_6 results in lower velocities and dynamic pressures for a given Mach number and Reynolds number and, therefore, lower power requirements and model loads than air (ref. 2). As early as 1945, Smelt (ref. 2) examined the possible use of SF_6 and other gases for use in wind tunnels because of the substantial reduction in tunnel power requirements that could be attained. It was estimated that the use of SF_6 would require only about 2 percent of the power required for operating a similar facility with air.

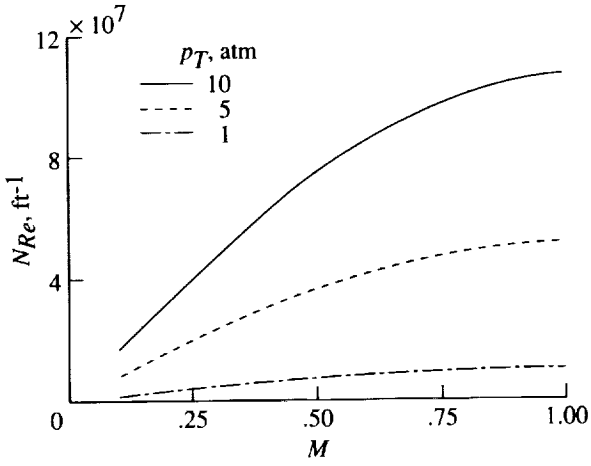

Figure 1. Attainable Reynolds numbers per foot as a function of Mach number for several stagnation pressures and a stagnation temperature of 70°F (294 K).

The major concern with the use of SF_6 in wind tunnels is that it does not behave thermodynamically in the same manner as air so that its use for compressible flows requires careful interpretation in order to apply SF_6 results to those in air. Under most conditions, air can be treated as both thermally and calorically perfect ($p = \rho RT$ and C_p and C_v are constants) so that the internal energy and speed of sound are functions of temperature alone. On the other hand, SF_6 generally behaves as a nonideal gas whose properties depend on pressure as well as temperature. Even at low pressures where SF_6 behaves as an ideal gas ($p = \rho RT$ and $d\epsilon^\circ = C_v^\circ(T)\, dT$), the ratio of specific heats differs from that of air and is dependent on the temperature. (See ref. 3.)

Several indications of the nonideal nature of SF_6 can be seen from the compressibility factor, the bulk modulus, and the thermal expansion coefficient (ref. 4). The compressibility factor gives an indication as to the thermal imperfection of the gas and is defined as

$$Z = \frac{p}{\rho RT} \tag{2}$$

The bulk modulus K and the thermal expansion coefficient β are defined, respectively, as

$$K = \rho \left(\frac{\partial p}{\partial \rho}\right)_T \tag{3}$$

$$\beta = -\frac{1}{\rho}\left(\frac{\partial \rho}{\partial T}\right)_p \tag{4}$$

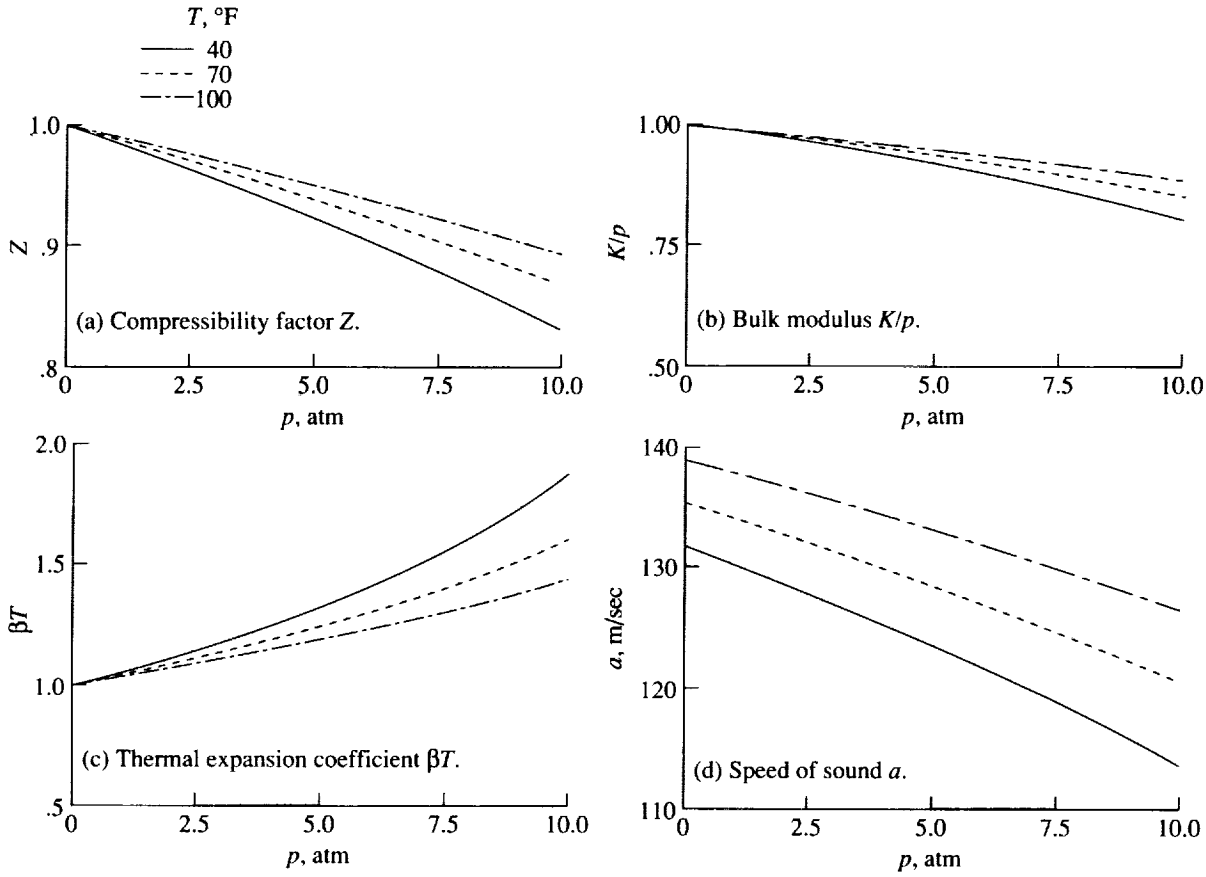

Figure 2. Thermodynamic variables of SF_6 as a function of pressure for several temperatures.

The bulk modulus is useful in determining the speed of sound which may be written as

$$a^2 = \frac{C_p K}{C_v \rho} \tag{5}$$

whereas the enthalpy can be defined in terms of the thermal expansion coefficient

$$dh = C_p\, dT + (1 - \beta T)\frac{dp}{\rho} \tag{6}$$

Note that for an ideal gas, the quantities Z, βT, and K/p are all unity, independent of the pressure. By examination of equations (5) and (6) along with the equation of state for an ideal gas ($p = \rho RT$), it is evident that neither the speed of sound nor the enthalpy varies with changes in pressure for an ideal gas. Plots of Z, K/p, and βT for SF_6 are shown as a function of pressure in figures 2(a), 2(b), and 2(c), respectively, for several temperatures. Figure 2(a) exemplifies the thermal imperfections of SF_6 in that the compressibility factor drops well below 1. At 40°F and a pressure of 5 atm, the compressibility factor is approximately 0.92 and continually drops as the pressure increases; at 10 atm, the compressibility factor is 0.83. Although higher temperatures result in compressibility factors nearer to unity, even at 100°F the compressibility factor is significantly lower than that of an ideal gas. Figures 2(b) and 2(c) indicate the extent to which changes in pressure affect K/p and βT and, thus, the speed of sound and enthalpy through equations (5) and (6). The speed of sound as a function of pressure is shown in figure 2(d) for temperatures of 40°F, 70°F, and 100°F.

As in the case of an ideal gas, the speed of sound decreases as the temperature is decreased. However, since SF_6 is a nonideal gas, the speed of sound drops significantly with increases in pressure. For a temperature of 100°F, a drop of about 9.5 percent is observed between 1 and 10 atm, whereas a drop of about 16 percent is seen for a temperature of 40°F over the same range of pressure. Note that this behavior is contrary to that of an ideal gas which has a speed of sound that is invariant with changes in pressure. Note also that as the pressure is reduced, Z, βT, and K/p all approach unity, indicating that

SF_6 behaves like an ideal gas at low pressures as expected.

Computational Procedure

For studying the aerodynamic effects caused by the use of SF_6, numerical solutions to the two-dimensional Euler and Navier-Stokes equations are obtained for airfoils at various flow conditions. For viscous calculations, the thin-layer approximation to the Navier-Stokes equations is used in the present analysis. The equations are written in generalized coordinates and conservation form as

$$\frac{\partial}{\partial t}(\mathbf{Q}) + \frac{\partial}{\partial \xi}(\mathbf{F}) + \frac{\partial}{\partial \eta}(\mathbf{G} - \mathbf{G}_v) = 0 \tag{7}$$

$$\mathbf{Q} = \frac{\tilde{Q}}{J} = \frac{1}{J}\begin{bmatrix} \tilde{\rho} \\ \tilde{\rho}\tilde{u} \\ \tilde{\rho}\tilde{v} \\ \tilde{E} \end{bmatrix} \tag{8}$$

$$\mathbf{F} = \frac{1}{J}\begin{bmatrix} \tilde{\rho}\tilde{U} \\ \tilde{\rho}\tilde{U}\tilde{u} + \xi_{\tilde{x}}\tilde{p} \\ \tilde{\rho}\tilde{U}\tilde{v} + \xi_{\tilde{y}}\tilde{p} \\ (\tilde{E} + \tilde{p})\tilde{U} \end{bmatrix} \tag{9}$$

$$\mathbf{G} = \frac{1}{J}\begin{bmatrix} \tilde{\rho}\tilde{V} \\ \tilde{\rho}\tilde{V}\tilde{u} + \eta_{\tilde{x}}\tilde{p} \\ \tilde{\rho}\tilde{V}\tilde{v} + \eta_{\tilde{y}}\tilde{p} \\ (\tilde{E} + \tilde{p})\tilde{V} \end{bmatrix} \tag{10}$$

$$\mathbf{G}_v = \frac{1}{J}\begin{bmatrix} 0 \\ \eta_{\tilde{x}}\tilde{\tau}_{\tilde{x}\tilde{x}} + \eta_{\tilde{y}}\tilde{\tau}_{\tilde{x}\tilde{y}} \\ \eta_{\tilde{x}}\tilde{\tau}_{\tilde{x}\tilde{y}} + \eta_{\tilde{y}}\tilde{\tau}_{\tilde{y}\tilde{y}} \\ \eta_{\tilde{x}}\tilde{\mathrm{b}}_{\tilde{x}} + \eta_{\tilde{y}}\tilde{\mathrm{b}}_{\tilde{y}} \end{bmatrix} \tag{11}$$

$$\left.\begin{aligned} \tilde{U} &= \xi_{\tilde{x}}\tilde{u} + \xi_{\tilde{y}}\tilde{v} \\ \tilde{V} &= \eta_{\tilde{x}}\tilde{u} + \eta_{\tilde{y}}\tilde{v} \end{aligned}\right\} \tag{12}$$

$$\tilde{p} = \tilde{p}\,(\rho, T) \tag{13}$$

The variables ξ and η correspond to the coordinates parallel and normal to the body surface, respectively. The variable $\tilde{Q}$ represents density, momentum, and total energy per unit volume, and the Jacobian J of the transformation is defined as

$$J = \frac{\partial(\xi, \eta)}{\partial(\tilde{x}, \tilde{y})} \tag{14}$$

In equation (11), $\tilde{b}_{\tilde{x}_i}$ is defined in tensor notation as

$$\tilde{\mathrm{b}}_{\tilde{x}_i} = \tilde{u}_j\tilde{\tau}_{\tilde{x}_i\tilde{x}_j} - \dot{q}_{\tilde{x}_i} \tag{15}$$

where the shear stress and heat-flux terms are given, respectively, by

$$\tilde{\tau}_{\tilde{x}_i\tilde{x}_j} = \frac{M_\infty}{N_{Re,\infty}}\left[\tilde{\mu}\left(\frac{\partial \tilde{u}_i}{\partial \tilde{x}_j} + \frac{\partial \tilde{u}_j}{\partial \tilde{x}_i}\right) + \tilde{\lambda}\frac{\partial \tilde{u}_k}{\partial \tilde{x}_k}\delta_{ij}\right] \tag{16}$$

$$\dot{q}_{\tilde{x}_i} = -\frac{M_\infty}{N_{Re,\infty}N_{Pr,\infty}}\frac{T_\infty C_{p,\infty}}{a_\infty^2}\tilde{k}\frac{\partial \tilde{T}}{\partial \tilde{x}_i} \tag{17}$$

The variables in the preceding equations have been nondimensionalized by introduction of the following quantities:

$$\left.\begin{aligned} \tilde{\rho} &= \frac{\rho}{\rho_\infty} & \tilde{x} &= \frac{x}{L} & \tilde{a} &= \frac{a}{a_\infty} & \tilde{T} &= \frac{T}{T_\infty} \\ \tilde{u} &= \frac{u}{a_\infty} & \tilde{y} &= \frac{y}{L} & \tilde{p} &= \frac{p}{\rho_\infty a_\infty^2} & \tilde{\mu} &= \frac{\mu}{\mu_\infty} \\ \tilde{v} &= \frac{v}{a_\infty} & \tilde{t} &= \frac{t a_\infty}{L} & \tilde{E} &= \frac{E}{\rho_\infty a_\infty^2} & \tilde{k} &= \frac{k}{k_\infty} \end{aligned}\right\} \tag{18}$$

Stokes' hypothesis for bulk viscosity, $\lambda + (2\mu/3) = 0$, is used. The molecular viscosity of air is computed using Sutherland's law (ref. 4), and the thermal conductivity is computed on the basis of a constant Prandtl number of 0.72. For SF_6, the viscosity is determined with a linear equation given by

$$\mu = 5.49 \times 10^{-8}T - 7.877 \times 10^{-7} \tag{19}$$

and the thermal conductivity is given by

$$k = 6.45291 \times 10^{-5}T^{0.942} \tag{20}$$

These equations are obtained from a technical bulletin supplied by General Chemical. Note that the dependence of the viscosity and thermal conductivity for SF_6 over a wide range of pressure is not accounted for. However, data given in reference 5 show that at 333 K, a difference of approximately 2.3 percent in the viscosity is observed between 1 and 11 atm.

For all turbulent calculations, the Baldwin-Lomax turbulence model is employed (ref. 6) where it should be noted that for both air and SF_6, the turbulent Prandtl number is assumed to be constant with a value of 0.8.

The equations are solved with an implicit, finite-volume, upwind-differenced algorithm in which the spatial derivatives of the fluxes are split into forward and backward contributions using flux-vector splitting so that type-dependent differencing can be used (ref. 7). The flux-vector splitting method used is that of Van Leer (ref. 8), with the modifications to the flux

formulas necessary for real-gas calculations given in reference 9.

For both the Euler and Navier-Stokes calculations, boundary conditions are applied explicitly at each iteration. On solid surfaces, no-slip and adiabatic wall-boundary conditions are used for viscous calculations and a no-flow condition normal to the body is enforced for inviscid calculations. In the far field, the pressure and density are determined using a locally one-dimensional characteristic analysis normal to the outer boundary, with the resulting expressions given by

$$p_b = \frac{1}{2}\left[(p_i + p_\infty + \rho_\infty a_\infty(\bar{u}_i - \bar{u}_\infty)\right] \quad (21a)$$

$$\rho_b = \rho_i + \frac{p_b - p_i}{a_\infty^2} \qquad (\bar{u} > 0) \quad (21b)$$

$$\rho_b = \rho_\infty + \frac{p_b - p_\infty}{a_\infty^2} \qquad (\bar{u} \le 0) \quad (21c)$$

where $\bar{u}$ denotes the velocity in the direction of the outward pointing normal to the far-field boundary. For SF_6, the temperature is then determined from the equation of state using Newton iteration and the internal energy is calculated using the procedure described below. For air, the internal energy is determined from perfect-gas laws.

The incorporation of nonideal-gas thermodynamics for SF_6 calculations is effected through the equation of state given by

$$p = \frac{RT}{v - d} + \sum_{i=2}^{5} \frac{\bar{a}_i + \bar{b}_i T + \bar{c}_i e^{-kT/T_c}}{(v - d)^i} \quad (22)$$

where the coefficients are given as (ref. 1)

$$k = 6.883022$$
$$T_c = 318.8 \text{ K}$$
$$d = 3.27367367 \times 10^{-4} \text{ m}^3/\text{kg}$$
$$\bar{a}_2 = -49.9051433 \text{ N-m}^4/\text{kg}^2$$
$$\bar{b}_2 = 5.485495 \times 10^{-2} \text{ N-m}^4/\text{kg}^2\text{-K}$$
$$\bar{c}_2 = -2.375924505 \times 10^{3} \text{ N-m}^4/\text{kg}^2$$
$$\bar{a}_3 = 4.124606 \times 10^{-2} \text{ N-m}^7/\text{kg}^3$$
$$\bar{b}_3 = -3.340088 \times 10^{-5} \text{ N-m}^7/\text{kg}^3\text{-K}$$
$$\bar{c}_3 = 2.819595 \text{ N-m}^7/\text{kg}^3$$
$$\bar{a}_4 = -1.612953 \times 10^{-5} \text{ N-m}^{10}/\text{kg}^4$$
$$\bar{b}_4 = 0$$
$$\bar{c}_4 = 0$$
$$\bar{a}_5 = -4.899779 \times 10^{-11} \text{ N-m}^{13}/\text{kg}^5$$
$$\bar{b}_5 = 1.094195 \times 10^{-11} \text{ N-m}^{13}/\text{kg}^5\text{-K}$$
$$\bar{c}_5 = -3.082731 \times 10^{-7} \text{ N-m}^{13}/\text{kg}^5$$

Equation (22) is valid over a temperature range from 200 K to 588 K and a pressure range from about 0.05 to 68 atm. Note that this is valid throughout the saturated region between 223 K and the critical point (318.65 K) as well as for the superheated region.

When needed, ideal-gas specific heats are determined from a curve fit of C_p° which is appropriate between temperatures of 200 K and 722 K and is given by (ref. 1)

$$C_p^\circ = C_1 + C_2 T + C_3 T^2 + C_4 T^3 + C_5/T^2 \quad (23)$$

where

$$C_1 = -107.9122479 \text{ J/kg-K}$$
$$C_2 = 3.94226447 \text{ J/kg-K}^2$$
$$C_3 = -5.128665 \times 10^{-3} \text{ J/kg-K}^3$$
$$C_4 = 2.422895 \times 10^{-6} \text{ J/kg-K}^4$$
$$C_5 = -9.602076433 \times 10^{5} \text{ J-K/kg}$$

Since all variables have been nondimensionalized by free-stream values, it is necessary to determine the reference density, speed of sound, and specific heat at constant pressure from the free-stream temperature and pressure. (Note that the free-stream temperature and pressure can be found from isentropic expansions from stagnation conditions to the desired free-stream Mach number using the technique given in the appendix.) Given the temperature and pressure in the free stream, the specific volume (and therefore the density) is determined from the equation of state using Newton iteration. The speed of sound is then calculated by

$$a^2 = \left(\frac{\partial p}{\partial \rho}\right)_S = \frac{C_p}{C_v}\left(\frac{\partial p}{\partial \rho}\right)_T = -\frac{v^2 C_p}{C_v}\left(\frac{\partial p}{\partial v}\right)_T \quad (24)$$

where (ref. 3)

$$C_v = C_v^\circ + T\int_\infty^v \left(\frac{\partial^2 p}{\partial T^2}\right)_v dv \quad (25)$$

$$C_p = C_v - \left[T \left(\frac{\partial p}{\partial T} \right)_v^2 \Big/ \left(\frac{\partial p}{\partial v} \right)_T \right] \tag{26}$$

For initializing the flow field, the total energy per mass is calculated by adding the kinetic energy to the internal energy in the free stream, $\epsilon(T, v)$, which is calculated from the departure function given by (ref. 3)

$$\epsilon(T,v) - \epsilon^\circ(T,v^\circ) = [A(T,v) - A^\circ(T,v^\circ)] + T\,[S(T,v) - S^\circ(T,v^\circ)] \tag{27}$$

where $\epsilon(T,v) - \epsilon^\circ(T,v^\circ)$, $A(T,v) - A^\circ(T,v^\circ)$, and $S(T,v) - S^\circ(T,v^\circ)$ are the differences between the internal energy, Helmholtz energy, and entropy, respectively, at the actual temperature and specific volume and a state at the same temperature but at a volume, $v^\circ = RT/p$, at which the gas obeys ideal-gas laws. The departure function for the Helmholtz energy and entropy are determined by (ref. 3)

$$A(T,v) - A^\circ(T,v^\circ) = -\int_\infty^v \left(p - \frac{RT}{v} \right) dv + RT\,\ln\left(\frac{v^\circ}{v} \right) \tag{28}$$

$$S(T,v) - S^\circ(T,v^\circ) = \frac{\partial}{\partial T} \int_\infty^v \left(p - \frac{RT}{v} \right) dv - R\,\ln\left(\frac{v^\circ}{v} \right) \tag{29}$$

Upon substitution of the equation of state into equations (27), (28), and (29), the final expression for the internal energy is obtained:

$$\epsilon(T,v) = \epsilon^\circ(T,v^\circ) + \sum_{i=2}^{5} \frac{\bar{a}_i + [1 + (kT/T_c)]\,\bar{c}_i e^{-kT/T_c}}{(i-1)(v-d)^{i-1}} \tag{30}$$

Note that the ideal internal energy $\epsilon^\circ(T, v^\circ)$ is actually a function only of temperature which is determined by integration of $C_v^\circ = C_p^\circ - R$ with respect to temperature using equation (23).

At each iteration of the flow solver, the density, velocity components, and total energy are obtained. The internal energy is easily calculated by subtraction of the kinetic energy from the total energy. Since the equation for the internal energy in the ideal-gas state $\epsilon^\circ(T, v^\circ)$ is a function only of temperature, equation (30) represents a nonlinear equation for the temperature that can be solved at each grid point using Newton iteration. From numerical experiments, it has been determined that the residual of the iteration procedure is reduced below 1.0×10^{-10} in only four iterations for all cases examined. Therefore, only four iterations are performed so that this procedure may be vectorized by the compiler. Once the iteration converges, the temperature is used in the equation of state along with the density to determine the pressure.

Note that for the present calculations, pure SF_6 is assumed. For calculations in air, the gas is assumed to be both thermally and calorically perfect.

Inviscid Results

Numerical Results for an NACA 0012 Airfoil

Inviscid calculations have been obtained for an NACA 0012 airfoil for both subsonic and transonic flow conditions. All the calculations are computed on a 129×41 O-type mesh that has been determined through a grid-refinement study using air to yield sufficiently accurate results. The outer boundary extent for this grid is approximately 20 chords and the average normal spacing near the body is about 7.7×10^{-3}. For each case, results obtained using SF_6 at several free-stream pressures and temperatures are compared with results for air. Note that calculations for air are not shown as a function of pressure since air is assumed to obey ideal-gas laws and is thus independent of the free-stream pressure.

The first case shown is an NACA 0012 airfoil at a free-stream Mach number of 0.63 and an angle of attack of 2°. Results for air as well as for SF_6 at free-stream pressures of 1 and 10 atm with a free-stream temperature of 70°F are shown in figure 3. As seen in figure 3(a), no difference is seen in the SF_6 pressure distributions at both 10 atm and 1 atm. In addition, little difference is apparent between the air and SF_6 pressure distributions. However, as shown in figure 3(b), the Mach number distribution over the surface of the airfoil is markedly different between the air and SF_6 calculations. For the air calculation, the maximum Mach number on the surface of the airfoil is approximately 0.947, whereas for the SF_6 calculations, the maximum Mach number decreases from 0.907 for the 1-atm case down to 0.873 for the 10-atm case.

It is interesting to note that for SF_6, the pressure coefficient at $M = 1$ (c_p^*) obtained from isentropic expansions is not only more negative than the corresponding c_p^* for air but gets increasingly negative as the pressure is increased. This dependence on pressure is contrary to that of air which is independent of free-stream pressure. An example of

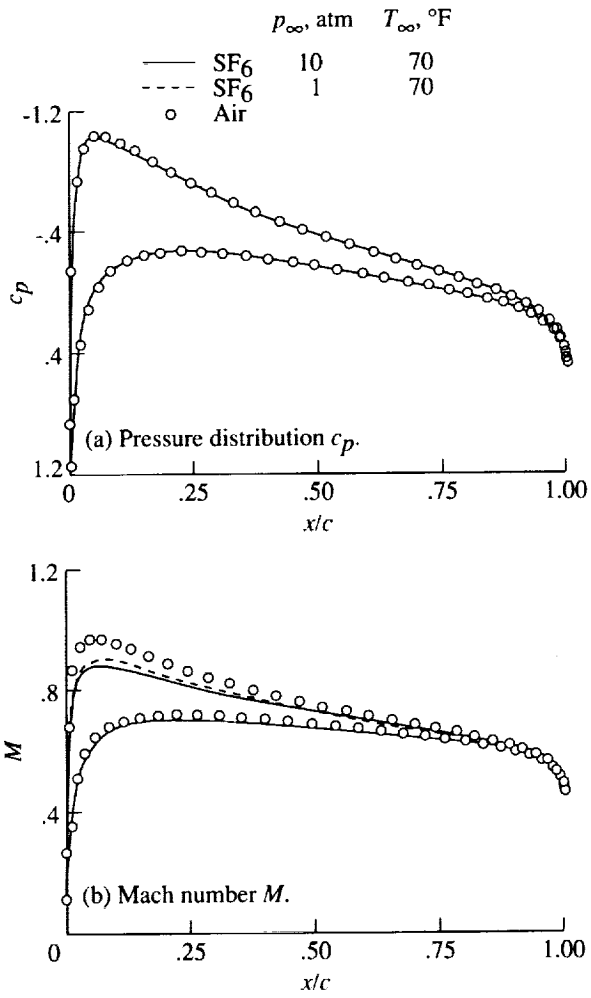

Figure 3. Comparison between air and SF_6 calculations for an NACA 0012 airfoil at $M_\infty = 0.63$ and $\alpha = 2°$.

this can be seen in figure 4 where a plot of c_p^* as a function of pressure is shown for SF_6 as well as for air. The free-stream Mach number for this example is 0.63 and the free-stream temperature is 70°F. Note that c_p^* for SF_6 is significantly lower (i.e., more negative) than that of air and continues to decrease as the pressure rises. Consequently, given equal local pressure coefficients and free-stream conditions, the maximum Mach number for SF_6 is dependent on the free-stream pressure as well as on the temperature and will be less than that of air.

Transonic calculations for an NACA 0012 airfoil at a free-stream Mach number of 0.8 and an angle of attack of 1.25° are shown in figure 5. The solution for these conditions in air has been calculated many times in the past and is characterized by a weak shock on the lower surface and a moderate shock on the upper surface. As expected, the SF_6 pressure

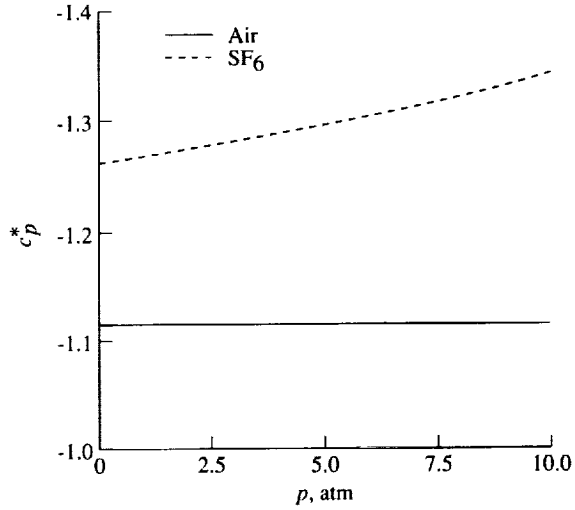

Figure 4. Effect of pressure on critical pressure coefficient for air and SF_6 at 70°F.

distributions do not agree with that of air. As seen in figure 5, the upper-surface shock for SF_6 moves increasingly forward on the airfoil as the free-stream pressure is increased from 1 to 10 atm and the lower-surface shock completely vanishes.

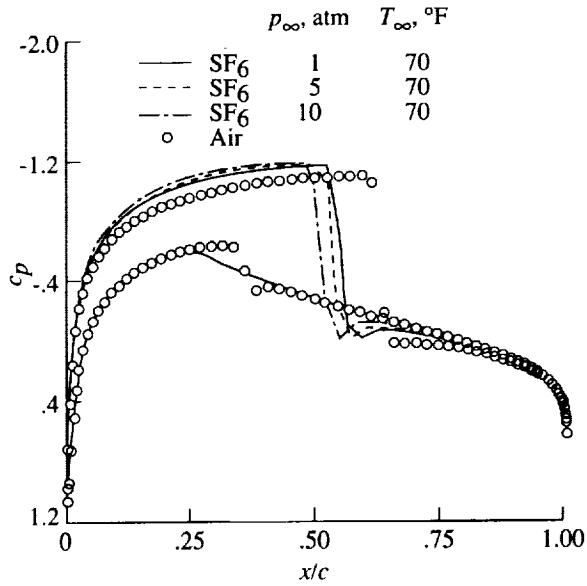

Figure 5. Comparison of pressure distributions between air and SF_6 for an NACA 0012 airfoil with $M_\infty = 0.8$ and $\alpha = 1.25°$.

Inviscid Scaling Procedures

Motivated by the results shown above, an attempt has been made to determine a systematic Mach number scaling procedure appropriate for use with SF_6 so that close agreement with air is obtained

for a wide array of pressure and temperature combinations. This is done by exploiting results from the small-disturbance theory through the use of the similarity parameter that is valid for subsonic, transonic, and supersonic flows with small disturbances (ref. 10). In the small-disturbance theory, the two-dimensional inviscid flow about an affine family of thin profiles is reduced to a one-parameter problem, namely,

$$\kappa = \frac{1 - M_\infty^2}{\left[\tau M_\infty^2(\gamma' + 1)\right]^{2/3}} \tag{31}$$

The similarity parameter κ combines the three parameters M_∞, γ', and τ. By using an appropriate definition of γ', a new free-stream Mach number can be obtained for use in the SF_6 calculations by matching the similarity parameter obtained for air. Afterward, the calculated lift and pressure coefficients can be corrected according to (ref. 10)

$$c_{l,\text{air}} = A c_{l,SF_6} \tag{32a}$$

$$c_{p,\text{air}} = A c_{p,SF_6} \tag{32b}$$

where

$$A = \frac{\gamma'_{SF_6} + 1}{\gamma_{\text{air}} + 1} \frac{M_{SF_6}^2}{M_{\text{air}}^2} \frac{1 - M_{\text{air}}^2}{1 - M_{SF_6}^2} \tag{33}$$

Four methods for calculating γ' based on free-stream conditions have been considered:

1. $\gamma' = \gamma = \left(\frac{C_p}{C_v}\right)_\infty$
2. $\gamma' = 1 + \left(\frac{p}{\rho\epsilon}\right)_\infty$
3. $\gamma' = \left(\frac{\rho a^2}{p}\right)_\infty$
4. $\gamma' = 2\Gamma_\infty - 1 = 1 + \left(\frac{\partial a^2}{\partial h}\right)_{S,\infty}$

where Γ is referred to as the fundamental derivative (ref. 11) and is given by

$$\Gamma = -\frac{v}{2} \frac{\left(\frac{\partial^2 p}{\partial v^2}\right)_S}{\left(\frac{\partial p}{\partial v}\right)_T} \tag{34}$$

The first method is simply the ratio of specific heats and is the actual definition of γ. The next three methods all revert to the ratio of specific heats for a perfect gas. However, for a real gas, the behavior of these quantities is not representative of the behavior of C_p/C_v. In particular, the "equivalent" γ's defined in methods 3 and 4 may drop below one at high pressure but are not indicative of the stability of the thermodynamic system.

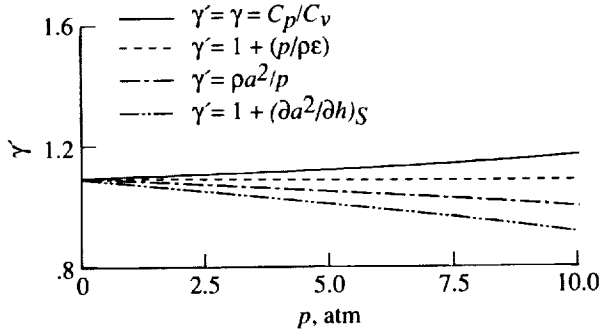

Figure 6. Variation of equivalent gammas with pressure for a temperature of 70°F.

The behavior of each definition of γ' for SF_6 is shown in figure 6 as a function of pressure for a fixed temperature of 70°F. The corresponding Mach number obtained from scaling considerations in order to obtain inviscid similarity with that of air at a Mach number of 0.8 is shown in figure 7 for each γ'. Note that for $\gamma' = 1 + (p/\rho\epsilon)_\infty$, the constant in the internal energy has been chosen so that at low pressure, the value of γ' agrees with the actual definition of $\gamma = C_p/C_v$.

As seen in figures 6 and 7, the value of $\gamma' = C_p/C_v$ increases as the pressure increases so that the net effect is to decrease the "equivalence" Mach number. From the pressure distribution shown in figure 5, it is evident that an increase in Mach number is required as the pressure increases so that use of this definition of γ' is inappropriate. Although method 2 decreases with increasing pressure, it is also not appropriate for scaling since this method does not have the flexibility to drop below one, which has been determined through numerical experiments to be necessary for proper agreement with air at high pressures. Method 3 is the isentropic expansion coefficient that may also be determined from isentropic expansions between two states very close to one another from which γ' may be calculated from the relation $p_1 v_1^{\gamma'} = p_2 v_2^{\gamma'}$. Figure 6 shows that this value drops faster with increasing pressure than method 2 so that the resulting Mach number shown in figure 7 is somewhat higher. Also, as required, this definition of γ' is not restricted to values greater than one.

The fourth method of determining γ' as seen in figures 6 and 7 decreases more rapidly with increasing pressure than the other methods so that the Mach number obtained is higher than that obtained with the other methods. The latter form of method 4 is of particular interest since its use in linearizing

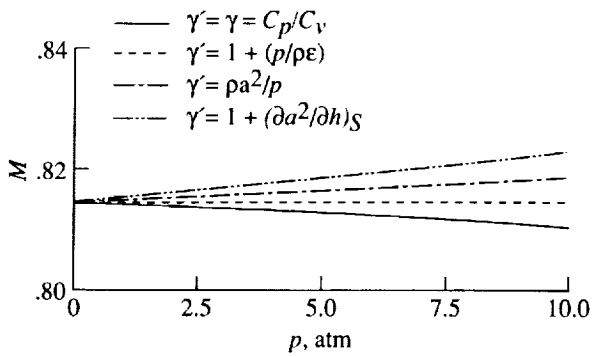

Figure 7. Resultant Mach numbers obtained with various equivalent gammas to achieve inviscid similarity with air at $M = 0.8$.

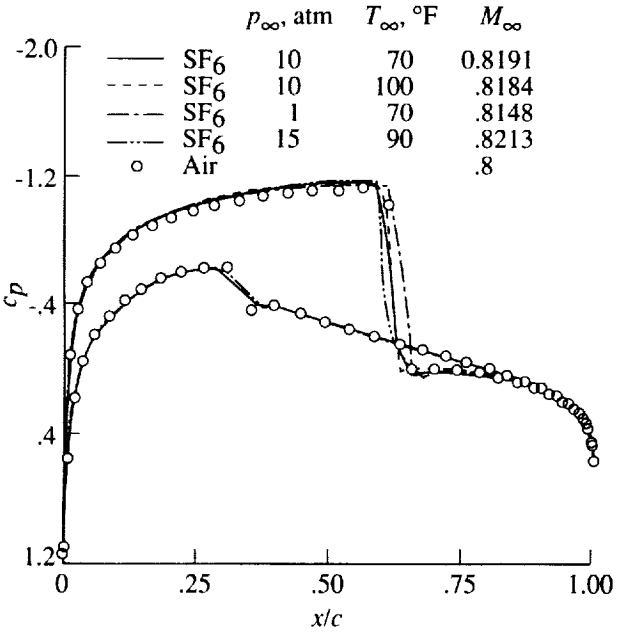

Figure 8. Effect of transonic scaling for SF_6 using $\gamma' = \rho a^2/p$ for an NACA 0012 airfoil with $M_\infty = 0.8$ (air) and $\alpha = 1.25°$.

the speed of sound in deriving the small-disturbance potential flow equation leads to an equation that is identical to that of an ideal gas but with γ' used in place of γ (ref. 12). The use of this definition of γ' should therefore be exact for scaling purposes in which the governing equations are based on the small-disturbance theory.

Results are shown in figure 8 where $\gamma' = \rho a^2/p$ has been used for scaling. Excellent agreement in shock location between air and SF_6 is obtained for a pressure of 10 atm and a temperature of 70°F. However, inconsistent shock locations are observed as the temperature and pressure are varied so that at 1 atm, the SF_6 shock location is aft of the air shock; whereas for 15 atm, the SF_6 shock location is forward of that of the air calculation.

Results are shown in figure 9 for the same case at several combinations of free-stream pressure and temperature in which the use of $\gamma' = 1 + (\partial a^2/\partial h)_S$ has been employed for Mach number scaling. The results show that for all cases considered, this definition of γ' leads to remarkably consistent results in that the shock locations are invariant with pressure and temperature changes and the agreement with air is good. In addition, as seen in figure 10, the comparison of air and SF_6 Mach number distributions over the airfoil is substantially improved upon applying the Mach number correction to the subcritical NACA 0012 airfoil case shown previously in figure 3. Because of its excellent consistency across a wide range of free-stream conditions, $\gamma' = 1 + (\partial a^2/\partial h)_S$ is used in all the following results in which scaling is applied.

Note that the scaling procedure described above is easily reversed; given the pressure, temperature, and Mach number in the free stream for SF_6, the equivalent Mach number for air is easily obtained. Also note that this scaling procedure is valid only for two-dimensional calculations; however, three-dimensional scaling laws exist but require modifications to the aspect ratio as well as to the Mach number.

It should also be emphasized that although the above results demonstrate the effectiveness of the inviscid scaling procedure for correlating SF_6 results with those of air, the procedure is strictly valid only for flows governed by the small-disturbance potential flow theory. However, from the results given above, it is evident that satisfactory results can be obtained in practice for flows not in strict adherence to the small-disturbance theory.

Another method that has been used for scaling, referred to as "streamline similarity," has been used experimentally for flows in Freon-12 (refs. 13 and 14). For this method the free-stream Mach number in an alternative test gas is determined so that the critical area ratio (A^*/A) matches that of air at the desired Mach number. Afterward, the pressure coefficients are modified by calculating A^*/A at each location on the body from which the corresponding Mach number and pressure coefficients in air can then be found. As seen in figure 11, the use of this technique for the present study yields an upper-shock location for a free-stream pressure of 1 atm that is slightly ahead of the air shock and results in poor resolution of the

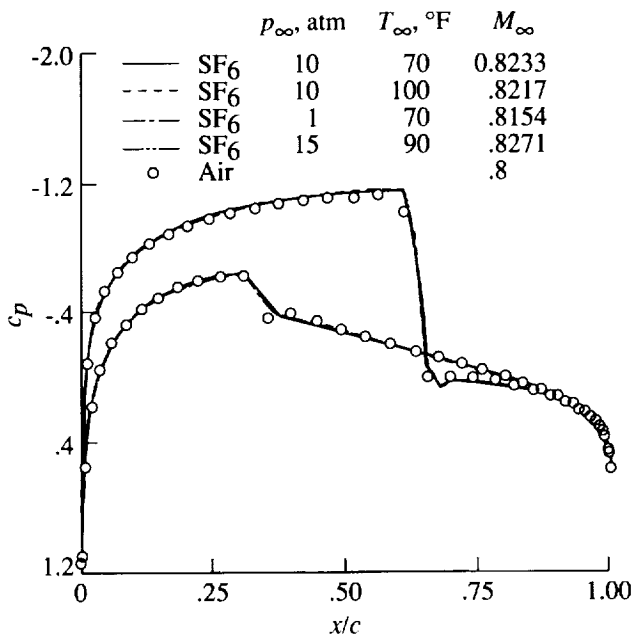

Figure 9. Effect of transonic scaling for SF_6 using $\gamma' = 1 + (\partial a^2/\partial h)_S$ for an NACA 0012 airfoil with $M_\infty = 0.8$ (air) and $\alpha = 1.25°$.

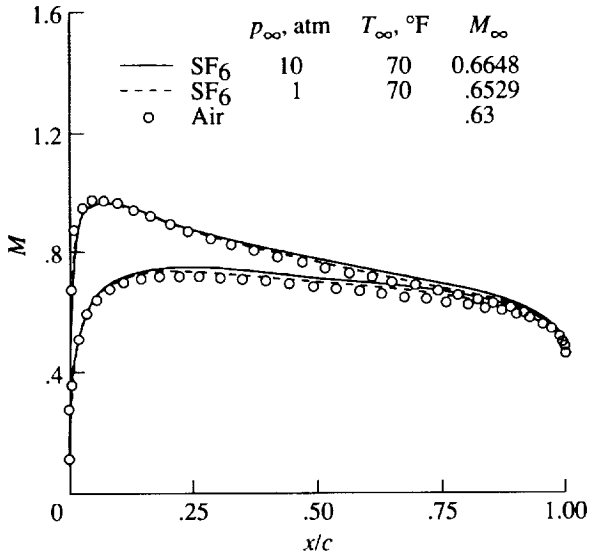

Figure 10. Mach number distributions for air and SF_6 after applying Mach number corections for an NACA 0012 airfoil with $M_\infty = 0.63$ (air) and $\alpha = 2°$.

lower-surface shock. This method also fails to give results consistent with those of air as the pressure and temperature are varied. Note in figure 11 that the pressure coefficients have not been corrected to corresponding air values since the inconsistent shock locations make this technique ineffective for the scaling of nonideal gases at high pressure. Also, the use of this process for experimental data requires that the pressure distribution over the entire configuration be known. In this manner, the pressures can be corrected and reintegrated in order to obtain corrected force and moment data.

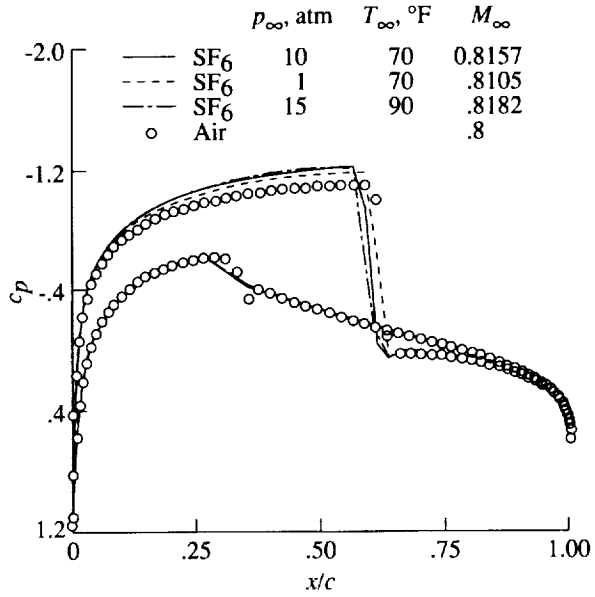

Figure 11. Effect of transonic scaling for SF_6 using streamline similarity for an NACA 0012 airfoil with $M_\infty = 0.8$ (air) and $\alpha = 1.25°$.

Viscous Calculations

Flat-Plate Calculations

Laminar and turbulent results for flow over a flat plate have been calculated using a computer program modified from that described in reference 15. Typical results are shown in figures 12 and 13 where ratios of SF_6 to air of several laminar boundary-layer parameters are shown. Figure 12 shows boundary-layer thickness, displacement thickness, momentum thickness, and skin-friction ratios over a Mach number range from 0.2 to 0.9 for free-stream conditions of 9 atm and 70°F. As seen from figure 12, the increase in boundary-layer thickness and displacement thickness due to an increase in Mach number is much less pronounced for SF_6 than for air. This difference can be in excess of 10 percent for the displacement thickness at Mach numbers on the order of one. The explanation of this can be illustrated by examining the behavior of a laminar boundary layer for an ideal gas with adiabatic-wall boundary conditions. The rate of change of the displacement thickness with Mach

number is approximately given by (ref. 10)

$$\frac{\partial\left(\delta^* N_{Re}^{1/2}/x\right)}{\partial M_\infty} \propto (\gamma - 1) M_\infty \qquad (35)$$

From this equation, it is evident that even at low pressures where SF_6 behaves as an ideal gas with $\gamma \approx 1.1$, the displacement thickness increases approximately four times faster with increasing Mach number for air ($\gamma = 1.4$) than for SF_6. Therefore, as the Mach number is increased, the differences between the air and SF_6 boundary layers may become very pronounced. Note also in figure 12 that the ratios of $\theta_{SF_6}/\theta_{air}$ and $c_{f,SF_6}/c_{f,air}$ increase slightly with increasing Mach number, which is the opposite trend from that seen for the boundary-layer and displacement thicknesses.

The variations of boundary-layer properties with pressure are shown in figure 13 for a free-stream Mach number of 0.8 and a temperature of 70°F. As seen in the figure, the effects of pressure changes on boundary-layer properties are small and are far less significant than those of Mach number. The greatest variation with pressure is seen in the displacement thickness which shows only a 0.58-percent difference in the ratios of SF_6 to air over a pressure range from 1 to 9 atm.

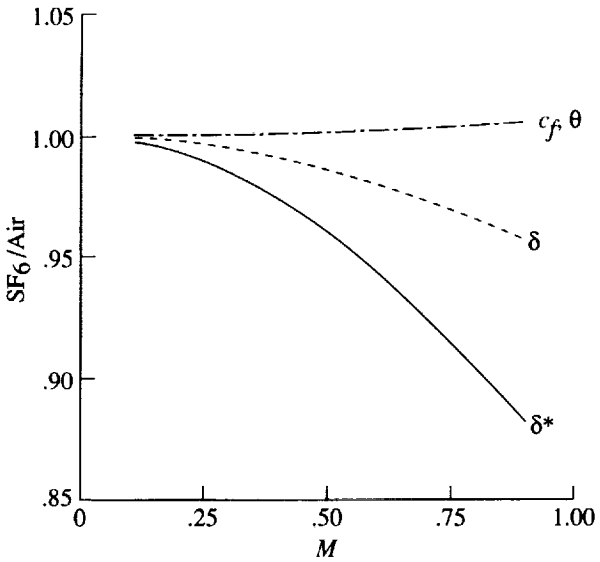

Figure 12. Comparison of flat-plate laminar boundary-layer parameters for air and SF_6 for several Mach numbers with $p_\infty = 9$ atm and $T_\infty = 70°F$.

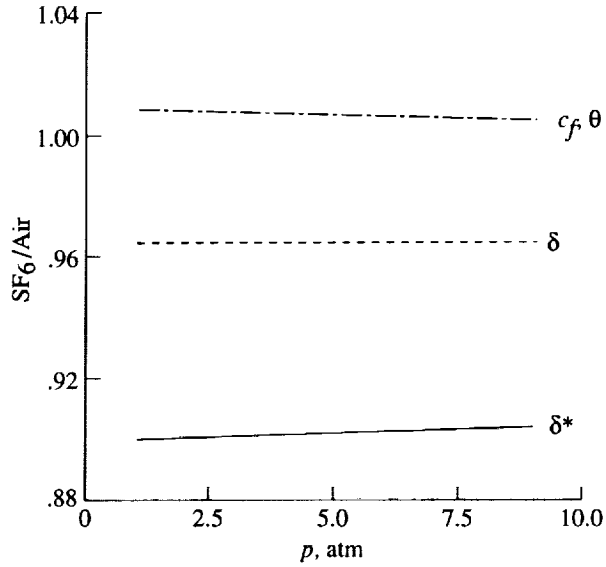

Figure 13. Comparison of flat-plate laminar boundary-layer parameters for air and SF_6 for several free-stream pressures with $M_\infty = 0.8$ and $T_\infty = 70°F$.

The flat-plate results obtained above indicate that differences in the boundary-layer thickness due to Mach number effects are much greater than those attributed to varying the free-stream pressure. Furthermore, since the Mach number corrections imposed on the inviscid flow field through the use of the scaling laws are relatively small and are certainly not large enough to significantly affect the thickness of the SF_6 boundary layer, it appears that the boundary-layer properties for flows in SF_6 will not agree with those of air except for the case of low Mach numbers. Although the matching of certain boundary-layer parameters can be achieved by using different Reynolds numbers for air and SF_6, the simultaneous matching of all parameters is not possible. For example, since both c_f and δ^*/x increase in inverse proportion to the square root of the Reynolds number, modification of the Reynolds number to match one of the parameters will degrade the correlation of the other. Although not shown, the variation of boundary-layer properties for turbulent flow over a flat plate behaves similarly.

Viscous Airfoil Calculations

A series of turbulent results have been obtained for flows over the Royal Aircraft Establishment (RAE) 2822 and NACA 0012 airfoils. All calculations are shown for 265 × 101 C-type meshes with 181 points on the surface of the airfoil, a far-field extent of 20 chords away from the body, and an average spacing normal to the body of approximately 2×10^{-6}. These parameters have been found to give

essentially grid-converged results by calculating flows on successively finer grids. The first case presented is that for flow over the RAE 2822 airfoil at a Mach number of 0.2, a Reynolds number of 6.5×10^6, and an angle of attack of 2.54°. The free-stream temperature and pressure are chosen to be 70°F and 10 atm, respectively, and the transition location is fixed at 3 percent chord. Comparisons between the air and SF_6 skin frictions are shown in figure 14. Because of the low Mach number, the skin frictions are in very good agreement between the air and SF_6 calculations, thus indicating that the flow is essentially incompressible. The calculated lift coefficients for air and SF_6 differ by 0.55 percent and are 0.537 and 0.540, respectively. Note that because of the nearly incompressible nature of this case, no Mach number correction is required for the SF_6 calculation.

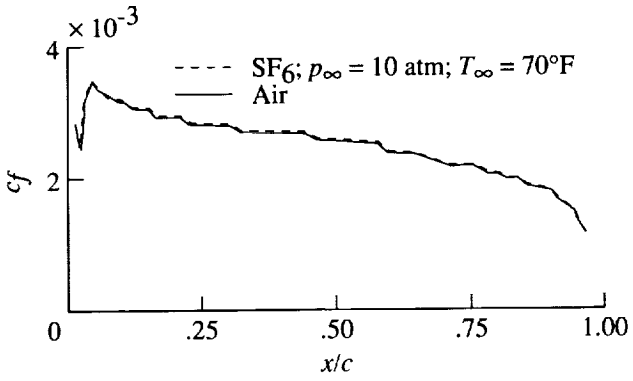

Figure 14. Skin-friction coefficients for air and SF_6 for RAE 2822 airfoil with $M_\infty = 0.2$, $\alpha = 2.54°$, and $N_{Re} = 6.5 \times 10^6$.

The next case considered is a compressible flow over the RAE 2822 airfoil in which no shocks are present. Results for both air and SF_6 with a free-stream pressure of 10 atm and a temperature of 70°F are compared with experimental values (ref. 16) for air in figures 15–17 for a Reynolds number of 5.7×10^6 and an angle of attack of 1.93°. For this case, transition is fixed at 3 percent chord which is the location at which transition strips were placed experimentally. The free-stream Mach number for air is 0.676 which agrees with that of experiment. Because of compressibility effects, the Mach number used for SF_6 is adjusted through the use of the inviscid scaling procedure and is determined to be 0.7086 based on $\gamma' = 0.9179$ calculated for the current free-stream conditions. Only small differences are observed between the calculated air and SF_6 pressure coefficients over the surface of the airfoil. In addition, the agreement in pressure distributions between the computed values and experimental data is seen to be

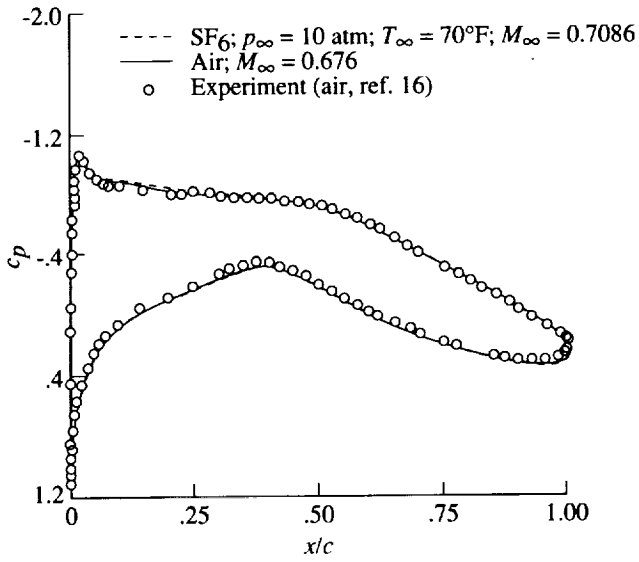

Figure 15. Calculated pressure coefficients for air and SF_6 compared with experimental data in air for RAE 2822 airfoil with $M_\infty = 0.676$ (air), $\alpha = 1.93°$, and $N_{Re} = 5.7 \times 10^6$.

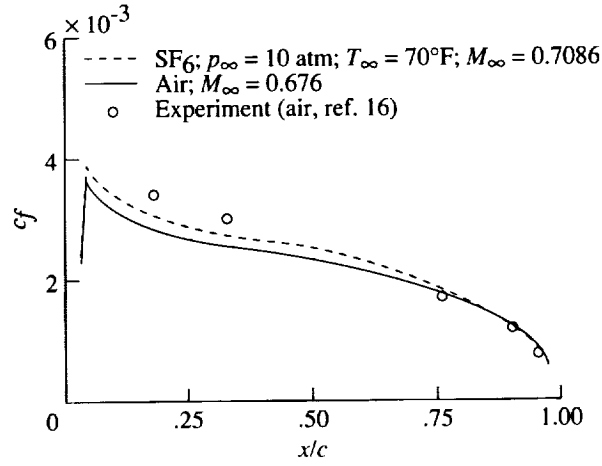

Figure 16. Calculated skin-friction coefficients for air and SF_6 compared with experimental data in air for an RAE 2822 airfoil with $M_\infty = 0.676$ (air), $\alpha = 1.93°$, and $N_{Re} = 5.7 \times 10^6$.

good. Examination of the skin friction and displacement thickness, however, reveals differences arising from compressibility. As with the flat-plate results, the skin-friction coefficient is higher for SF_6 than for air, whereas the displacement thickness is somewhat less.

Transonic results are shown for the RAE 2822 airfoil in figures 18 and 19 for a Reynolds number of 6.5×10^6 and an angle of attack of 2.54°. For this case, SF_6 results at several combinations of free-stream

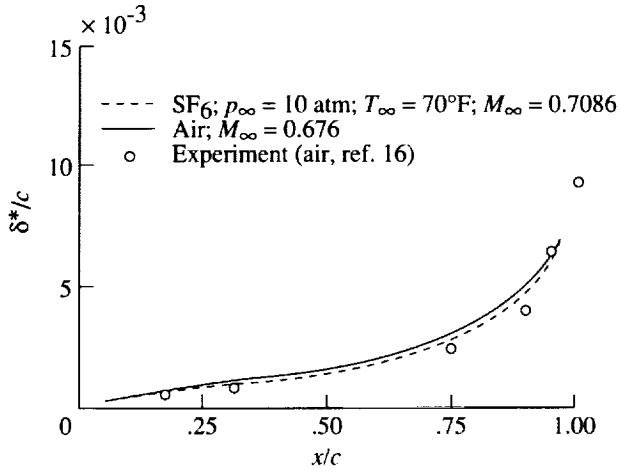

Figure 17. Calculated displacement thickness for air and SF_6 compared with experimental data in air for an RAE 2822 airfoil with $M_\infty = 0.676$ (air), $\alpha = 1.93°$, and $N_{Re} = 5.7 \times 10^6$.

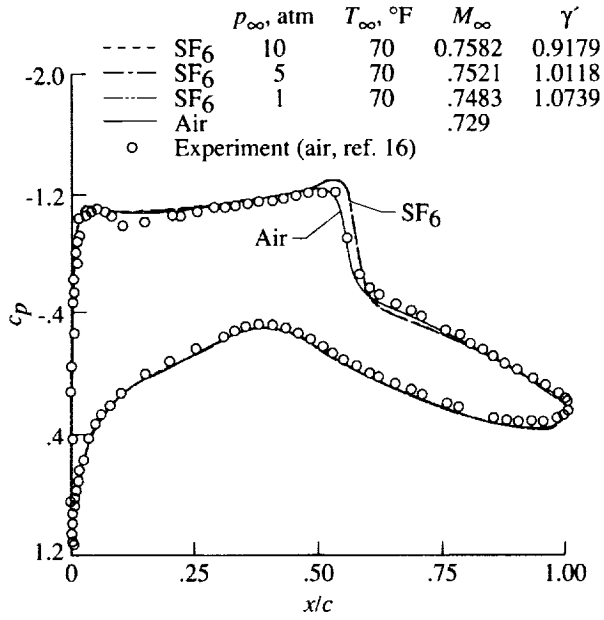

Figure 18. Calculated pressure coefficients for air and SF_6 compared with experimental data in air for an RAE 2822 airfoil with $M_\infty = 0.729$ (air), $\alpha = 2.54°$, and $N_{Re} = 6.5 \times 10^6$.

temperature and pressure are compared with air calculations as well as with experimental data. Note that for each free-stream temperature and pressure, a different Mach number is required for each of the SF_6 calculations in order to achieve inviscid similarity with air at a Mach number of 0.729. The value of γ' used for each of the calculations is given in figure 18 along with the resulting pressure distributions.

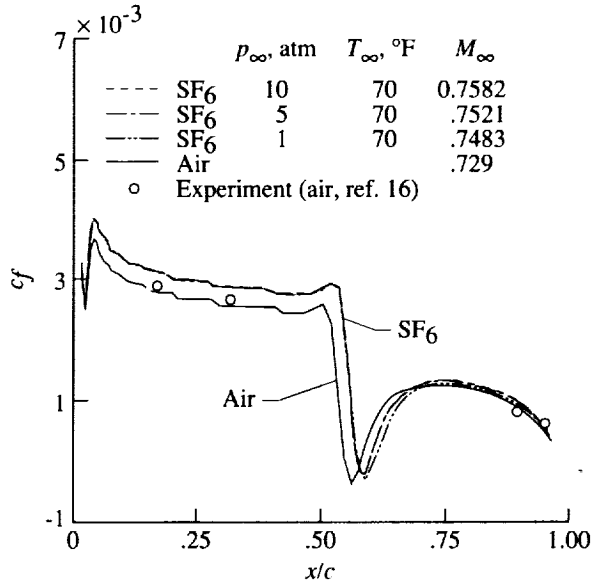

Figure 19. Calculated skin-friction coefficients for air and SF_6 compared with experimental data in air for an RAE 2822 airfoil with $M_\infty = 0.729$ (air), $\alpha = 2.54°$, and $N_{Re} = 6.5 \times 10^6$.

Because of the Mach number scaling applied to each of the SF_6 cases, the results for all the SF_6 calculations agree very well with each other in spite of the variations in free-stream pressure and temperature. The shock location for the air calculation agrees well with the experimental data and is somewhat ahead of the SF_6 shock locations. This discrepancy can be attributed to two sources. First, careful examination of figure 20, which depicts inviscid results for this case, shows that although good agreement in shock location is achieved by scaling the Mach number for SF_6 based on free-stream conditions, the shock calculated is slightly aft of that for air and the reexpansion behind the shock is noticeably different. Second, since the boundary layer for SF_6 is thinner than that for air, the flow outside the boundary layer "sees" a slightly thinner geometry which results in less movement upstream of the shock because of boundary-layer displacement effects. Skin-friction results for each of the SF_6 cases are compared with those of air along with experimental data in figure 19. Ahead of the shock, all the SF_6 skin frictions appear to be very close to each other but are higher than the air values. At the shock, the skin friction for both air and SF_6 indicate a small region of separation.

In addition to the results obtained above, viscous results using both air and SF_6 have been obtained and compared with experimental data (refs. 17 and 18) for the NACA 0012 airfoil at a Reynolds

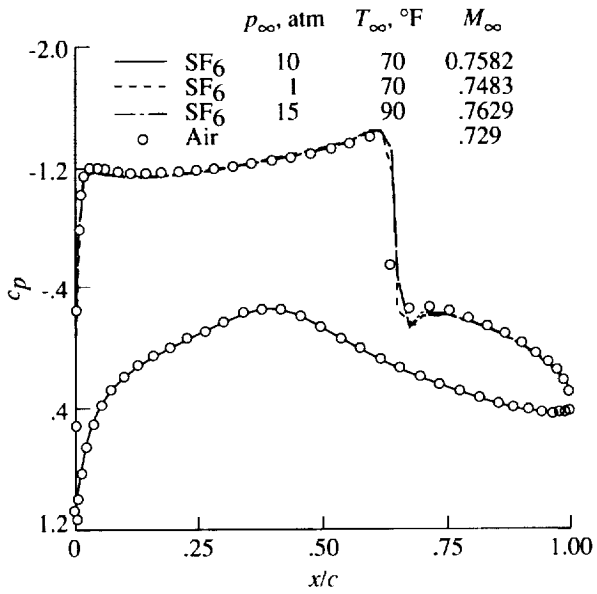

Figure 20. Calculated pressure coefficients for air and SF_6 (inviscid) for an RAE 2822 airfoil with $M_\infty = 0.729$ (air) and $\alpha = 2.54°$.

number of 6×10^6 and a free-stream Mach number of 0.3500 (air). For the calculations that follow, emphasis is placed on determining the highest angle of attack at which steady lift values can be obtained. In this manner, general conclusions may be made as to the relative accuracy that can be achieved by substituting SF_6 in place of air for determining conditions near maximum lift. Although the free-stream Mach number is relatively low, high Mach numbers may occur locally on the body because of the high angle of attack. It should be noted that the last angle of attack for which steady lift can be maintained is not the same as that occurring at maximum lift for the airfoil. The maximum lift condition is generally an unsteady phenomenon and is determined experimentally by averaging data over a finite time period.

A comparison of calculated and experimental lift coefficients as a function of angle of attack is shown in figure 21 for air. Experimental data of Ladson (ref. 17) is shown by the solid line, whereas the symbols denote computational values. The dashed line represents the experimental data of Harris after applying the suggested angle-of-attack correction (ref. 18). As seen, the computational and experimental results agree well up to about 10.5°, which is the last angle of attack for which steady lift values could be obtained computationally.

However, as seen in figure 22, SF_6 calculations at the same Mach number and a free-stream temperature of 70°F yield steady solutions up to $\alpha = 11.5°$ for a free-stream pressure of 10 atm. For a free-stream pressure of 1 atm, shown in figure 23, steady lift could be obtained up to 11°. It is apparent that for SF_6, the maximum angle of attack for steady lift is greater than that of air and is dependent on the free-stream conditions. This is attributed to the fact that as the free-stream temperature and pressure are changed, the maximum local Mach numbers on the airfoil are also altered. For example, the maximum Mach number in the field for the air calculations at $\alpha = 10.5°$ is about 1.3, whereas the maximum Mach number for the SF_6 case at 70°F and 10 atm is only about 1.08 and at 1 atm is approximately 1.14.

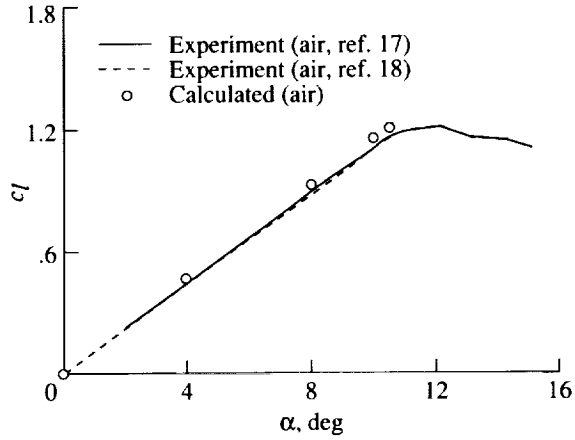

Figure 21. Comparison of lift plotted against angle of attack between calculations (air) and experimental data (air) for an NACA 0012 airfoil with $M_\infty = 0.3500$ and $N_{Re} = 6.0 \times 10^6$.

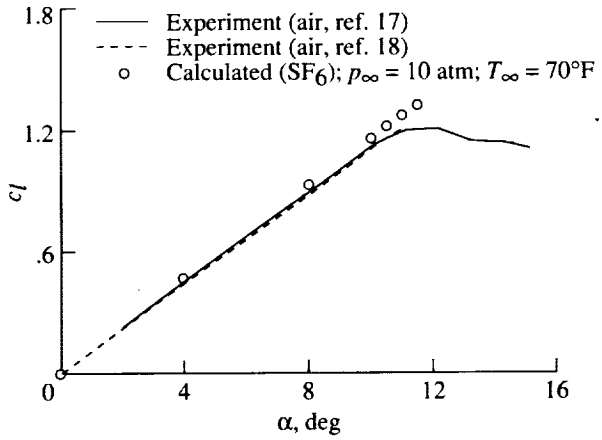

Figure 22. Comparison of lift plotted against angle of attack between experimental data (air) and calculations (SF_6) at $p_\infty = 10$ atm and $T_\infty = 70°F$ for an NACA 0012 airfoil with $M_\infty = 0.3500$ and $N_{Re} = 6.0 \times 10^6$.

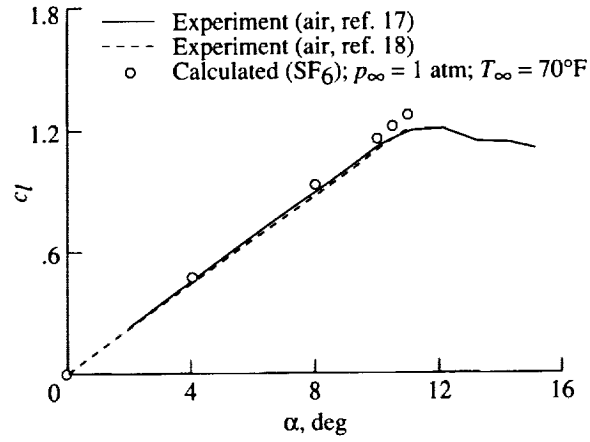

Figure 23. Comparison of lift plotted against angle of attack between experimental data (air) and calculations (SF_6) at $p_\infty = 1$ atm and $T_\infty = 70°F$ for an NACA 0012 airfoil with $M_\infty = 0.3500$ and $N_{Re} = 6.0 \times 10^6$.

Mach number corrections to the SF_6 calculations have been applied to both the 1- and 10-atm cases. The resulting free-stream Mach numbers for the two cases are 0.3715 ($\gamma' = 1.074$) for the 1-atm case and 0.3833 ($\gamma' = 0.9179$) for the 10-atm case. Figures 24 and 25 show the lift curves for the 10- and 1-atm cases, respectively, obtained by performing the calculations at the scaled Mach numbers. With the Mach number corrections, the maximum angle of attack for which steady lift could be obtained was 10.5° for the 10-atm case at 70°F, which is in agreement with that obtained for air. For the 1-atm case, however, steady lift could be achieved at an angle of attack of 10.75° which is slightly greater than that for air.

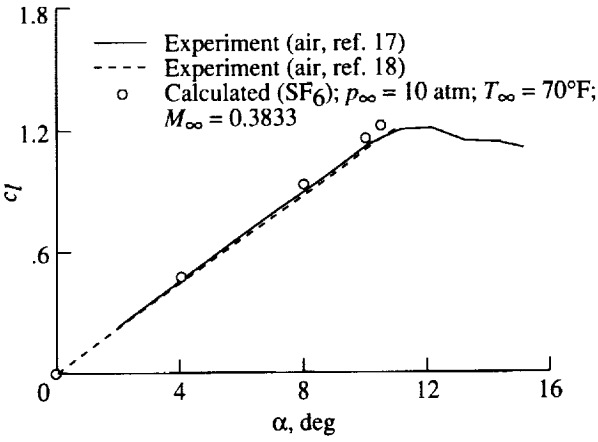

Figure 24. Comparison of lift plotted against angle of attack between experimental data (air) and calculations (SF_6) using Mach number scaling for an NACA 0012 airfoil with $M_\infty = 0.3500$ (air) and $N_{Re} = 6.0 \times 10^6$.

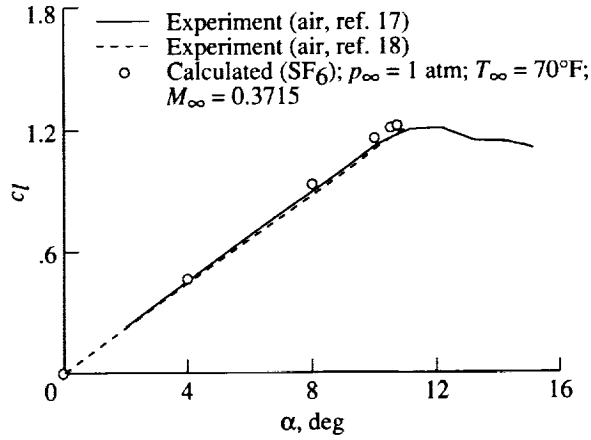

Figure 25. Comparison of lift plotted against angle of attack between experimental data (air) and calculations (SF_6) using Mach number scaling for an NACA 0012 airfoil with $M_\infty = 0.3500$ (air) and $N_{Re} = 6.0 \times 10^6$.

Comparisons of upper-surface skin frictions between air and SF_6 at an angle of attack of 10.5° are shown in figure 26(a) for the 10-atm case and in figure 26(b) for the 1-atm case. Air results are shown in each figure along with SF_6 at both the corrected and uncorrected Mach numbers. Without the Mach number correction, the skin frictions for SF_6 at both 1 and 10 atm are in poor agreement with that of air. A small separated region near the leading edge of the airfoil that is present in the air calculation is completely absent for both of the SF_6 calculations obtained at the uncorrected Mach number. Good agreement is seen for SF_6 using the scaled Mach numbers with the extent of separation matched well, although differences in the skin friction still remain at about 10 percent chord for the 1-atm case.

Computed pressure distributions for air and SF_6 are compared with experimental data (ref. 18) in figure 27 for an angle of attack of 10°. The SF_6 pressure distributions have been corrected for correlation with air. As seen, the air and SF_6 calculations agree quite well with each other as well as with the experimental data.

The pressure distributions over the first 12 percent of the airfoil at an angle of attack of 10.5° are shown in figure 28 for air and for the 10-atm SF_6 case with and without the Mach number correction. It is seen that with the Mach number correction, the minimum c_p for SF_6 occurring at the nose is in good agreement with that of air. On the contrary, the pressure coefficient obtained without the Mach number correction is not in such close agreement with air. It is evident that for these cases, a Mach number correction is very helpful even though the free-stream Mach number is relatively low.

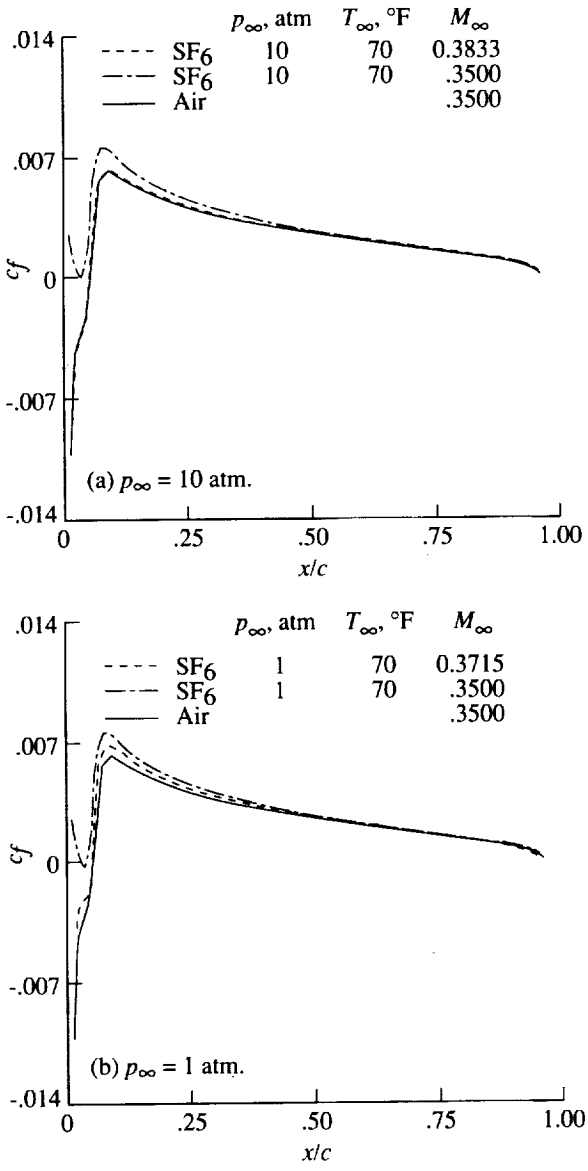

Figure 26. Skin-friction coefficients for air and SF_6 computed at two different pressures with and without Mach number corrections for an NACA 0012 airfoil with $\alpha = 10.5°$ and $N_{Re} = 6.0 \times 10^6$.

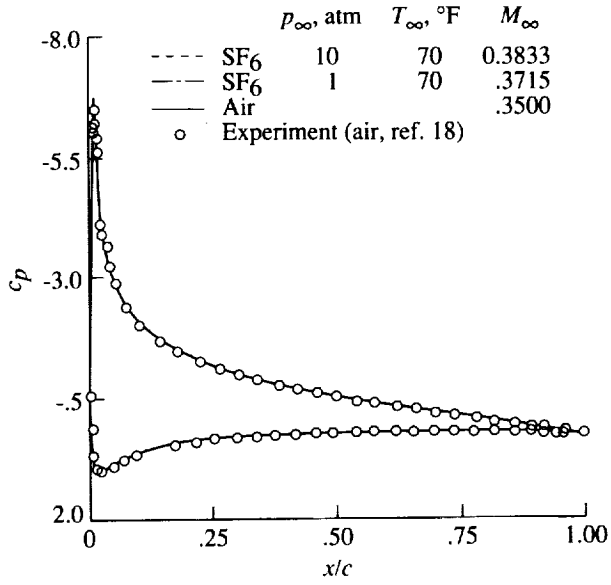

Figure 27. Calculated pressure distributions for air and SF_6 compared with experimental data (air) for an NACA 0012 airfoil with $\alpha = 10°$ and $N_{Re} = 6.0 \times 10^6$.

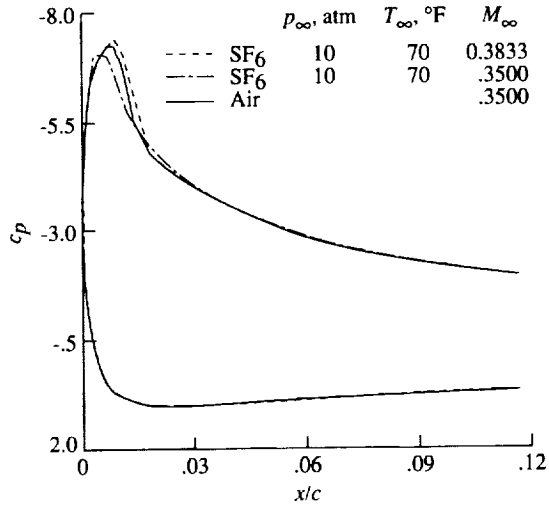

Figure 28. Calculated pressure distributions near leading edge for air and SF_6 computed with and without Mach number corrections for an NACA 0012 airfoil with $\alpha = 10.5°$ and $N_{Re} = 6.0 \times 10^6$.

Finally, in figures 29 and 30 comparisons are shown for air at a Mach number of 0.3185 and an angle of attack of 11.5° with those for SF_6 at a Mach number of 0.3500 and the same angle of attack. The Mach number for the air calculation has been determined through the use of Mach number scaling in order to verify that the SF_6 results at a Mach number of 0.3500 can be used to find those of air at an alternate Mach number. Recall that for air at a Mach number of 0.3500, the maximum angle of attack at which a steady solution could be obtained was 10.5°. With Mach number scaling, however, the Mach number is sufficiently reduced so that a steady lift can now be obtained at $\alpha = 11.5°$. As seen in figures 29 and 30, both the pressure distributions and skin frictions agree well between air and SF_6. Note that for this comparison, the SF_6 pressures have been modified according to the scaling procedure to correlate with those in air at a Mach number of 0.3185.

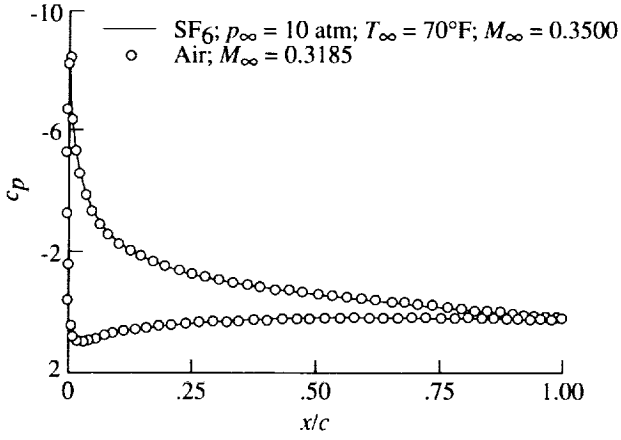

Figure 29. Calculated pressure coefficients for air and SF_6 at 10 atm for an NACA 0012 airfoil with $M_\infty = 0.3185$ (air), $M_\infty = 0.3500$ (SF_6), $\alpha = 11.5°$, and $N_{Re} = 6.0 \times 10^6$.

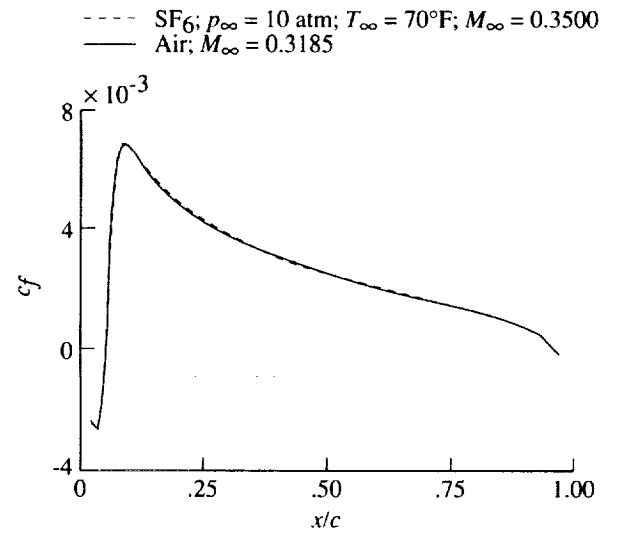

Figure 30. Calculated skin-friction coefficients for air and SF_6 at 10 atm for an NACA 0012 airfoil with $M_\infty = 0.3185$ (air), $M_\infty = 0.3500$ (SF_6), $\alpha = 11.5°$, and $N_{Re} = 6.0 \times 10^6$.

Concluding Remarks

A study has been conducted to examine several aspects of using sulfur hexafluoride (SF_6) as a substitute for air in wind tunnels in order to conduct testing at high Reynolds numbers. An attempt has been made in the current study to examine some of the differences introduced and to demonstrate a Mach number scaling procedure that is essential in obtaining good correlation between air and SF_6 results, particularly for transonic flows with shocks.

The main problems stemming from the use of SF_6 are that for compressible flows, neither the shock locations nor the boundary-layer parameters agree with that of air. It is shown in the current study that the first problem can be effectively compensated for by the use of a Mach number scaling that is based on the small-disturbance theory using an "equivalent" gamma calculated from properties in the free stream. For inviscid transonic flows, this has been shown to give consistently good agreement between air and SF_6 over a range of free-stream temperatures and pressures.

Since the impetus for high Reynolds number testing is to match the boundary-layer parameters to those at flight Reynolds numbers, the biggest problem in using SF_6 is that for flows in which compressibility is significant, the variation of boundary-layer parameters with Mach number is different between air and SF_6. This is very important for shock/boundary-layer interactions and for determining conditions near maximum lift. In the latter case, calculations at high angles of attack and low Mach numbers using both air and SF_6 have been made in order to determine the maximum angle of attack at which steady lift can be obtained. It is shown that this angle of attack for air and SF_6 do not agree and that the results for SF_6 are dependent on the free-stream conditions. However, significant improvement can be obtained in comparing air and SF_6 results by applying a Mach number scaling. This has the effect of correcting the inviscid portion of the flow field that is instrumental in determining boundary-layer properties.

Computations for flow over an RAE 2822 airfoil were made to show the effect of Mach number. For a low Mach number where the flow is essentially incompressible, no difference is observed between the skin frictions calculated for air and SF_6. As the Mach number is increased, the boundary layer for air becomes thicker than that of SF_6 and boundary-layer displacement effects are more pronounced. For a transonic case at which SF_6 calculations are obtained for three combinations of free-stream temperature and pressure, differences in the shock location between air and SF_6 are seen. These are attributed to the thinner boundary layer for SF_6 and to the fact that the Mach number scaling does not give exact agreement, even for inviscid cases.

Although exact agreement between air and SF_6 at a given Reynolds number cannot generally be attained for all Mach numbers, the use of SF_6 at high Reynolds numbers may still yield more fruitful information than extrapolated results from air data at lower Reynolds numbers. In general, it should be

expected that good agreement with air can be obtained for incompressible or nearly incompressible flows. As the Mach number is increased, the correlations in boundary-layer parameters should be expected to deteriorate because of thermodynamic differences between the gases.

The suitability of employing SF_6 for testing high-lift devices can currently be determined only through experiments. This is due to the uncertainty in transition locations between air and SF_6 which is very important in determining the performance of the high-lift system. Also, since the flow field around high-lift systems is greatly dependent on the gap settings between the elements, good agreement of the boundary-layer parameters with those of air is essential. Unfortunately, the flow can reach locally high Mach numbers between the elements of the high-lift system even though the free-stream Mach number may be low.

NASA Langley Research Center
Hampton, VA 23665-5225
February 28, 1991

Appendix

Isentropic Expansions for Sulfur Hexafluoride

Isentropic expansions are often necessary for determining relationships between two states at different Mach numbers. For these calculations, the total enthalpy and entropy are the same at both states:

$$H = h + \frac{u^2}{2} = \epsilon + pv + \frac{M^2a^2}{2} = \text{Constant} \quad \text{(A1)}$$

$$S(v_2, T_2) - S(v_1, T_1) = 0 \quad \text{(A2)}$$

Note that for SF_6, the internal energy necessary for determining the enthalpy is expressed as a function of temperature and specific volume by equation (30). An expression for the difference in entropy can be obtained as a sum of differences between the states shown in figure 31 and is given by

$$\begin{aligned} S(v_2, T_2) - S(v_1, T_1) = {} & S(v_2, T_2) - S^\circ(v_b^\circ, T_b) \\ & + S^\circ(v_b^\circ, T_b) - S^\circ(v_a^\circ, T_a) \\ & + S^\circ(v_a^\circ, T_a) - S(v_1, T_1) \end{aligned} \quad \text{(A3)}$$

The difference in entropy between states (v_2, T_2) and (v_b°, T_b) is determined using the departure function for entropy that is given by equation (29). After substitution of the equation of state into equation (29), this difference is given by

$$\begin{aligned} S(v_2,T_2) - S^\circ(v_b^\circ, T_b) = {} & -R \ln\left(\frac{v_2}{v_2 - d}\right) \\ & - \sum_{i=2}^{5} \frac{\bar{b}_i - \left(k/T_c\bar{c}_i e^{-kT_2/T_c}\right)}{(i-1)(v_2 - d)^{i-1}} \\ & - R \ln\left(\frac{v_b^\circ}{v_2}\right) \end{aligned} \quad \text{(A4)}$$

A similar expression is obtained for the difference in entropy between states (v_a°, T_a) and (v_1, T_1). Note that between (v_b°, T_b) and (v_a°, T_a), the gas is considered to behave as an ideal gas so that the difference in entropy between these two states (which are at the same specific volume) can be expressed as

$$S^\circ(v_b^\circ, T_b) - S^\circ(v_a^\circ, T_a) = \int_a^b \frac{C_v^\circ}{T} dT \quad \text{(A5)}$$

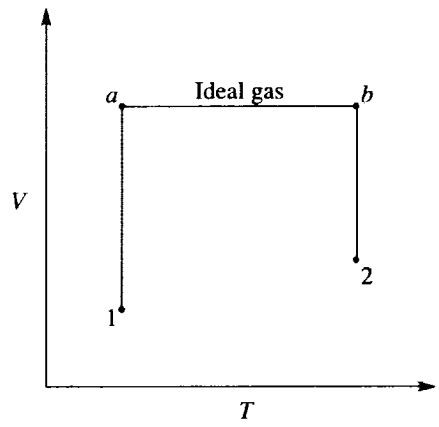

Figure 31. Representative states for determining changes in thermodynamic properties.

By using equations (A3)–(A5) along with the equation of state and the curve fit of C_p° given by equation (23), the statement of constant entropy between states 1 and 2 is given by

$$\begin{aligned} S_2 - S_1 = {} & -R \ln\left(\frac{v_1 - d}{v_2 - d}\right) \\ & + (C_1 - R) \ln\left(\frac{T_2}{T_1}\right) + C_2(T_2 - T_1) \\ & + \frac{C_3}{2}(T_2^2 - T_1^2) + \frac{C_4}{3}(T_2^3 - T_1^3) \\ & - \frac{C_4}{2}\left(\frac{1}{T_2^2} - \frac{1}{T_1^2}\right) \\ & - \sum_{i=2}^{5} \frac{\bar{b}_i - \left(k/T_c\bar{c}_i e^{-kT_2/T_c}\right)}{(i-1)(v_2 - d)^{i-1}} \\ & + \sum_{i=2}^{5} \frac{\bar{b}_i - \left(k/T_c\bar{c}_i e^{-kT_1/T_c}\right)}{(i-1)(v_1 - d)^{i-1}} = 0 \end{aligned} \quad \text{(A6)}$$

The procedure used in the current study for the isentropic expansions is a "divide and conquer" algorithm in which the specific volume is used as an iteration parameter. Two initial values of the specific volume (v_1 and v_2) are assumed so that when the temperatures T_1 and T_2 are obtained using the condition of constant entropy, the total enthalpy calculated from (v_1, T_1) and the desired Mach number will be higher than the actual total enthalpy, whereas the conditions at (v_2, T_2) will yield a total enthalpy that is lower than the desired value. Note that the desired value of the total enthalpy is obtained from the reference temperature, pressure, and Mach number. The average value of the two initial guesses of the specific volume is then used to obtain a specific

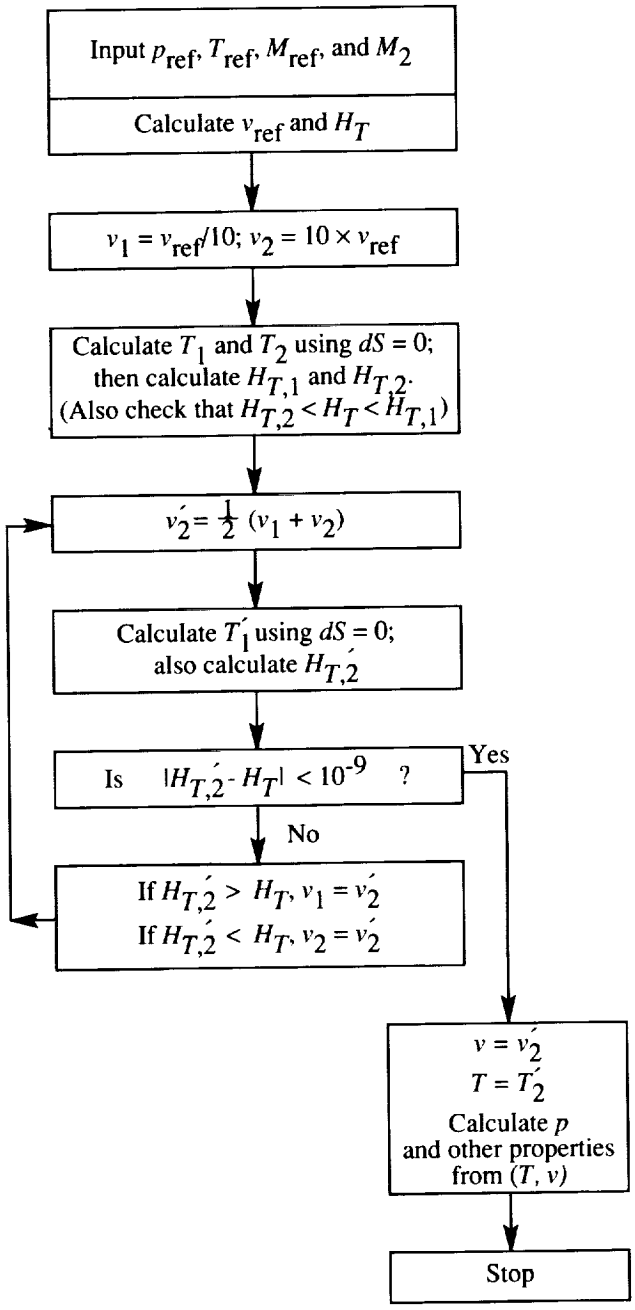

Figure 32. Procedure for determining isentropic expansion between two states.

volume that is between the two previous ones. The temperature T_2' is obtained from equation (A6) using Newton iteration, and the total enthalpy is calculated from (v_2', T_2') and the Mach number at which the conditions are sought. If the resulting total enthalpy is higher than the actual value desired, the current specific volume replaces the previous value of v_1. Conversely, if the total enthalpy is lower than that desired, then v_2 is replaced with the current value of specific volume. The values of v_1 and v_2 are again averaged together and the process is repeated until the total enthalpy at the desired Mach number is the same as that at the reference conditions. Note that the condition of constant entropy is automatically satisfied through the use of equation (A6). For further clarity, a summary of the technique is shown in figure 32.

Sample results are shown in figure 33 where isentropic expansions for SF_6 are compared with those of air for Mach numbers up to 1. For the calculations in figure 33, the reference condition is chosen as stagnation with a temperature of 70°F. Results are shown for air and for SF_6, which has results for both 10 and 1 atm. The figure indicates that both the pressure and temperature drop more rapidly for air than for SF_6 as the Mach number increases. The density, however, changes slightly more rapidly for SF_6 than for air.

Since the procedure described above is applicable for isentropically expanding between states at any two Mach numbers, several properties can be calculated in addition to finding conditions in the test section of a wind tunnel from the stagnation conditions. For example, the value of $\gamma' = 1 + (\partial a^2/\partial h)_S$ can easily be obtained by expanding between two Mach numbers that are very close to one another. Although $\gamma' = 1 + (\partial a^2/\partial h)_S$ can be calculated analytically from the equation of state, isentropic expansions can be used as a check that the thermodynamic and algebraic manipulations have been done correctly. Also, for given free-stream conditions, the value of c_p^* can be easily determined by expanding from the free-stream Mach number to $M = 1$. Conversely, given the free-stream conditions and a value of c_p, the local Mach number can be determined in regions of the flow that have the same entropy and total enthalpy as the free stream.

The effects on isentropic expansions of changing the stagnation conditions are also interesting to note. For an isentropic expansion from stagnation conditions to a given Mach number, both the temperature and pressure decrease as the Mach number increases. Although decreases in temperature result in a lower speed of sound, recall from figure 2(d) that decreases in pressure lead to an increase in the speed of sound. At low pressures where the gas behaves ideally, the increase in Mach number leads to a decrease in the speed of sound because of the decrease in temperature. However, at a high stagnation pressure as the Mach number is increased, the increase in speed of sound due to the decrease in pressure dominates over the decrease in speed of sound due to decreasing temperature. The net effect is that for

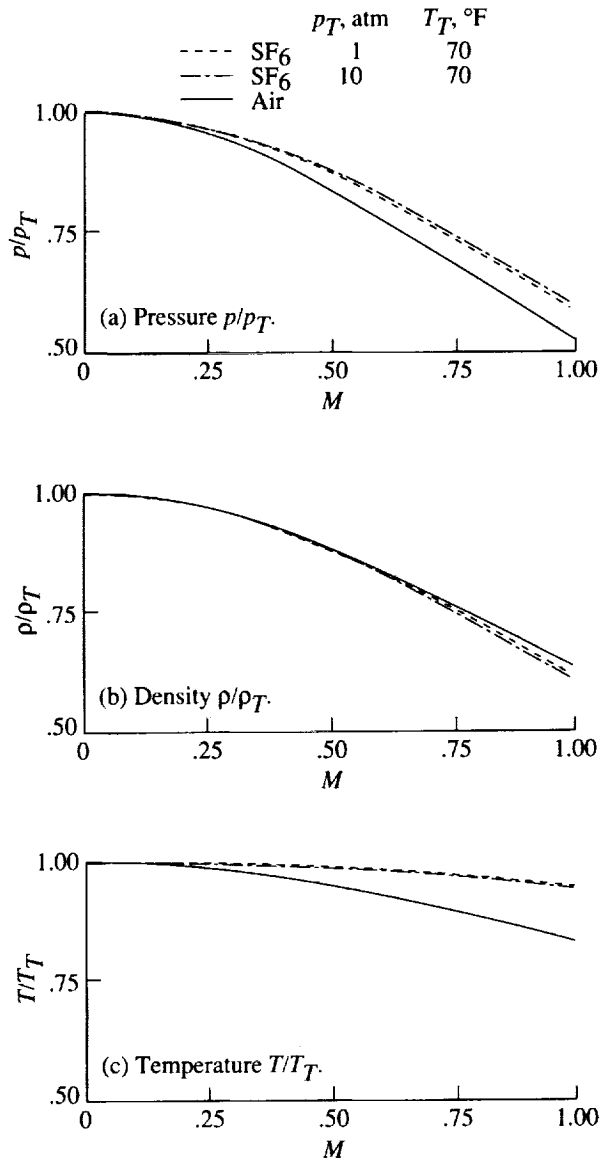

Figure 33. Variation of pressure, density, and temperature with Mach number for air and SF_6 determined from isentropic expansions.

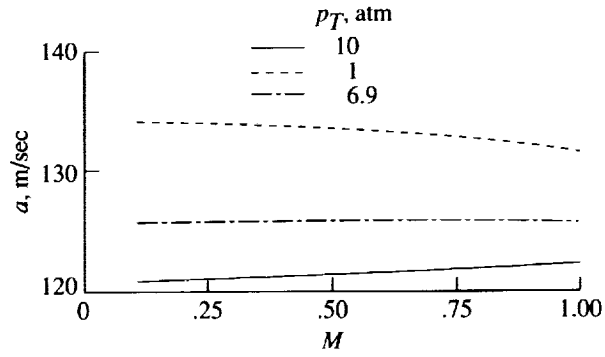

Figure 34. Speed of sound for SF_6 as a function of Mach number for various stagnation conditions at $T_T = 70°F$.

high stagnation pressures, the speed of sound also increases as the Mach number increases. Since a drop in pressure and temperature have opposite effects on the speed of sound, stagnation conditions can be found that will result in a speed of sound that varies only slightly over a fairly wide Mach number range. This occurs when the fundamental derivative given in equation (34) becomes unity so that $(\partial a^2/\partial h)_S$ vanishes.

Plots of the speed of sound as a function of Mach number are shown in figure 34 for several combinations of stagnation pressure and temperature. For a stagnation pressure of 1 atm and a stagnation temperature of 70°F, it is seen that as the Mach number increases, the speed of sound is reduced. This trend is the same as that observed for an ideal gas such as air. At stagnation conditions of 10 atm and 70°F, however, an increase in the speed of sound is observed as the Mach number is increased to $M = 1$ because of the decrease in pressure. For stagnation conditions of 6.9 atm and 70°F, the speed of sound is seen to be essentially constant with a variation of only about 0.1 percent over the Mach number range considered. For these stagnation conditions, $(\partial a^2/\partial h)_S$ varies from about -0.02 at $M = 0.2$ up to a value of 0.02 at $M = 1$.

References

1. SF_6. SFBR-1, Allied Chemical Corp., c.1976. (Replaces SFBR-1 dated 1973.)

2. Smelt, R.: *Power Economy in High-Speed Wind Tunnels by Choice of Working Fluid and Temperature.* Rep. No. Aero. 2081, British Royal Aircraft Establ., Aug. 1945.

3. Modell, Michael; and Reid, Robert C.: *Thermodynamics and Its Applications,* Second ed. Prentice-Hall, Inc., c.1974.

4. White, Frank M.: *Viscous Fluid Flow.* McGraw-Hill, Inc., c.1974.

5. Hoogland, J. H. B.; Van Den Berg, H. R.; and Trappeniers, N. J.: Measurements of the Viscosity of Sulfur Hexafluoride up to 100 Bar by a Capillary-Flow Viscometer. *Physica,* vol. 134A, no. 1, Dec. 1985, pp. 169–192.

6. Baldwin, Barrett; and Lomax, Harvard: Thin-Layer Approximation and Algebraic Model for Separated Turbulent Flows. AIAA Paper 78-257, Jan. 1978.

7. Anderson, W. Kyle; Thomas, James L.; and Van Leer, Bram: Comparison of Finite Volume Flux Vector Splitting for the Euler Equations. *AIAA J.,* vol. 24, no. 9, Sept. 1986, pp. 1453–1460.

8. Van Leer, Bram: Flux-Vector Splitting for the Euler Equations. *Eighth International Conference on Numerical Methods in Fluid Dynamics,* E. Krause, ed., *Volume 170 of Lecture Notes in Physics,* Springer-Verlag, 1982, pp. 507–512.

9. Grossman, B.; and Walters, R. W.: An Analysis of Flux-Split Algorithms for Euler's Equations With Real Gases. *A Collection of Technical Papers—AIAA 8th Computational Fluid Dynamics Conference,* June 1987, pp. 177–186. (Available as AIAA-87-1117.)

10. Liepmann, H. W.; and Roshko, A.: *Elements of Gasdynamics.* John Wiley & Sons, Inc., c.1957.

11. Thompson, P. A.; and Lambrakis, K. C.: Negative Shock Waves. *J. Fluid Mech.,* vol. 60, pt. 1, Aug. 21, 1973, pp. 187–208.

12. Wagner, Bernhard; and Schmidt, Wolfgang: Theoretical Investigations of Real Gas Effects in Cryogenic Wind Tunnels. *AIAA J.,* vol. 16, no. 6, June 1978, pp. 580–586.

13. Von Doenhoff, Albert E.; Braslow, Albert L.; and Schwartzberg, Milton A.: *Studies of the Use of Freon-12 as a Wind-Tunnel Testing Medium.* NACA TN 3000, 1953.

14. Pozniak, O. M.: *Investigation Into the Use of Freon 12 as a Working Medium in a High-Speed Wind-Tunnel.* Note No. 72, College of Aeronautics, Cranfield (England), Nov. 1957.

15. Miner, E. W.; Anderson, E. C.; and Lewis, Clark H.: *A Computer Program for Two-Dimensional and Axisymmetric Nonreacting Perfect Gas and Equilibrium Chemically Reacting Laminar, Transitional and-or Turbulent Boundary Layer Flows.* VPI-E-71-8 (Contract NAS1-9337), Dep. of Aerospace Engineering, Virginia Polytechnic Inst., Jan. 1975. (Available as NASA CR-132601.)

16. Cook, P. H.; McDonald, M. A.; and Firmin, M. C. P.: Aerofoil RAE 2822—Pressure Distributions, and Boundary Layer and Wake Measurements. *Experimental Data Base for Computer Program Assessment,* AGARD-AR-138, May 1979, pp. A6-1–A6-77.

17. Ladson, Charles L.: *Effects of Independent Variation of Mach and Reynolds Numbers on the Low-Speed Aerodynamic Characteristics of the NACA 0012 Airfoil Section.* NASA TM-4074, 1988.

18. Harris, Charles D.: *Two-Dimensional Aerodynamic Characteristics of the NACA 0012 Airfoil in the Langley 8-Foot Transonic Pressure Tunnel.* NASA TM-81927, 1981.

NASA
National Aeronautics and Space Administration

Report Documentation Page

1. Report No.	2. Government Accession No.	3. Recipient's Catalog No.
NASA TP-3086		

4. Title and Subtitle	5. Report Date
Numerical Study of the Aerodynamic Effects of Using Sulfur Hexafluoride as a Test Gas in Wind Tunnels	May 1991
	6. Performing Organization Code
7. Author(s)	8. Performing Organization Report No.
W. Kyle Anderson	L-16849
9. Performing Organization Name and Address	10. Work Unit No.
NASA Langley Research Center Hampton VA 23665-5225	505-60-01-01
	11. Contract or Grant No.
12. Sponsoring Agency Name and Address	13. Type of Report and Period Covered
National Aeronautics and Space Administration Washington, DC 20546-0001	Technical Paper
	14. Sponsoring Agency Code

15. Supplementary Notes

16. Abstract

A numerical study is presented that investigates some aerodynamic consequences of using sulfur hexafluoride (SF_6) as a test gas in wind tunnels. Inviscid results for airfoils indicate that the shock location calculated for SF_6 is vastly different from that in air for transonic cases. As the free-stream pressure is increased for a given free-stream temperature and Mach number, and real-gas effects become more pronounced, the shock moves progressively forward on the airfoil. Good correlation, however, can be obtained between SF_6 and air even for pressures at which nonideal-gas effects are significant by altering the free-stream SF_6 Mach number using a Mach number scaling procedure. Computations for subsonic turbulent flows over an NACA 0012 airfoil show that the maximum angle of attack at which steady lift can be obtained is different between air and SF_6. In addition, for SF_6 this angle of attack depends greatly on the free-stream conditions. However, close agreement with air can be achieved at low subsonic Mach numbers by altering the free-stream Mach number according to the inviscid scaling procedure. Conversely, calculated viscous results show that even with Mach number scaling at transonic Mach numbers, the shock location and skin-friction values calculated between air and SF_6 are in disagreement. This is attributed to the limitations of the scaling procedure and to the thinner boundary layer for SF_6.

17. Key Words (Suggested by Author(s))	18. Distribution Statement
Computational aerodynamics Wind-tunnel testing	Unclassified—Unlimited Subject Category 02

19. Security Classif. (of this report)	20. Security Classif. (of this page)	21. No. of Pages	22. Price
Unclassified	Unclassified	24	A03

NASA FORM 1626 OCT 86

NASA-Langley, 1991

For sale by the National Technical Information Service, Springfield, Virginia 22161-2171